Space Sci Rev (2021) 217:10
https://doi.org/10.1007/s11214-020-00776-6

# Proton Aurora and Optical Emissions in the Subauroral Region

**B. Gallardo-Lacourt**[1,2] · **H.U. Frey**[3] · **C. Martinis**[4]

Received: 5 November 2019 / Accepted: 27 November 2020 / Published online: 6 January 2021


**Abstract** Optical structures located equatorward of the main auroral oval often exhibit different morphologies and dynamics than structures at higher latitudes. In some cases, questions arise regarding the formation mechanisms of these photon-emitting phenomena. New developments in space and ground-based instruments have enabled us to acquire a clearer view of the processes playing a role in the formation of subauroral structures. In addition, the discovery of new optical structures helps us improve our understanding of the latitudinal and altitudinal coupling that takes place in the subauroral region. However, several questions remain unanswered, requiring the development of new instruments and analysis techniques. We discuss optical phenomena in the subauroral region, summarize observational results, present conclusions about their origin, and pose a number of open questions that warrant further investigation of proton aurora, detached subauroral arcs and spots, stable auroral red (SAR) arcs, and STEVE (Strong Thermal Emission Velocity Enhancement).

**Keywords** Optical structures · Subauroral region

## 1 Introduction

Proton aurora and the structures observed at subauroral latitudes occur in a region of magnetic field transition. In this region, Earth's magnetic field changes from a stretched topology closer to the auroral oval, into more dipolar field lines towards the equator. Optical structures in this region are diverse in morphology, propagation, dynamics, and lifetimes. In addition,

Auroral Physics
Edited by David Knudsen, Joe Borovsky, Tomas Karlsson, Ryuho Kataoka and Noora Partmies

✉ B. Gallardo-Lacourt

1 NASA Goddard Space Flight Center, Greenbelt, MD, USA

2 Universities of Space Research Association, Columbia, MD, USA

3 Space Sciences Laboratory, University of California, Berkeley, CA, USA

4 Center of Space Physics, Boston University, Boston, MA, USA

some of these structures exhibit different generation mechanisms than aurorae; specifically, some of these subauroral optical structures are not caused by the excitation from energetic particle precipitation as is the case with auroral arcs (Vegard 1932).

In this chapter, we review the recent advances made on proton aurora, detached subauroral arcs and spots, Subauroral Red (SAR) arcs, and the newly discovered phenomenon named STEVE (Strong Thermal Emission Velocity Enhancement). For each of these topics we provide a description of their main features, drivers and formation mechanisms. At the end of the chapter, we highlight some of the open questions that still remain for this region.

## 2 Proton Aurora

There are two common uses of the term "proton aurora". In some contexts, it is used to describe any aurora that is generated by energetic protons. As energetic electrons and protons interact with the atomic and molecular oxygen and nitrogen of Earth's upper atmosphere, ionization and excitation occur. Spectroscopic observations of photons generated by this process do not provide information weather the initial atomic excitation—and subsequent emission—was stimulated by energetic electrons or protons. Accordingly, the term "proton aurora" refers to excitation produced by energetic proton precipitation.

When spectroscopic data are used to determine the mean energy and flux of energetic electrons, it is almost always assumed that the relative contribution from protons is negligible (Germany et al. 1994; Galand and Lummerzheim 2004). One exception is the use of IMAGE-FUV data where the proton contribution could be determined and a proper correction to the electron contribution could be made (Frey et al. 2003). Another possibility is the use of a specific model and its comparison to measurement comparisons (Galand and Lummerzheim 2004). So, in this case additional measurements for instance by low-altitude satellites with particle detectors are required to determine the relative contribution of energetic protons to the overall aurora generation.

The other common use of the term "proton aurora" refers strictly to emission that comes from precipitating energetic protons themselves. Bare protons cannot emit any photons but during precipitation they can undergo charge exchange collisions with atmospheric constituents, briefly become neutral hydrogen atoms, and are then able to emit hydrogen-specific photons. The brightest and most prominent emissions are the Lyman-$\alpha$ at 121.57 nm in the ultraviolet and the Balmer-$\alpha$ and Balmer-$\beta$ lines at 656.3 and 486.1 nm in the visible, respectively. The process of charge exchange decouples the hydrogen atoms from the guiding magnetic field, at which point they will travel in straight lines (unless neutral-neutral collisions become important at low altitude) until their electron is stripped off and they become positively charged protons again (Fig. 1). This leads to a spatial broadening of any existing small-scale structure in the proton precipitation. The resulting proton aurora does not show fine structure and appears relatively homogeneous on spatial scales of $\sim$100 km (Fig. 2). Fang et al. (2004) found that the main dispersion region for a fine proton beam is located in the altitude range of around 250–450 km, where the first few charge exchange collisions typically occur. As the energetic protons move at high speed, the resulting hydrogen atoms emit photons with a specific Doppler shift and any emission is shifted towards blue if seen from the ground or towards red if seen from space (see e.g. Chamberlain 1961). High-resolution spectroscopic measurements then allow estimates of the proton energy (Galand and Chakrabarti 2006). High-resolution spectroscopic separation of the Doppler-shifted Lyman-$\alpha$ from the much brighter cold emission of the geocorona was the operational principle of the IMAGE Spectrographic Imager SI-12 proton aurora channel which allowed for

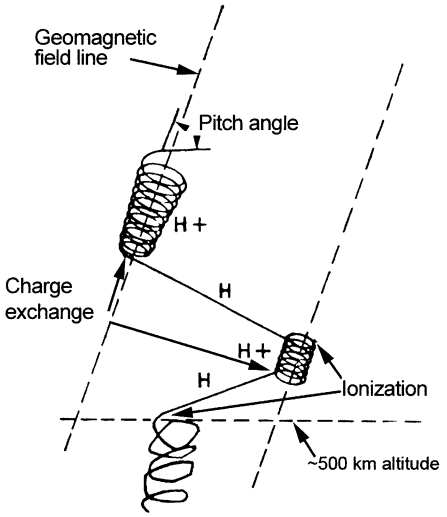


**Fig. 1** Schematic of the charge exchange process for energetic protons which become neutral hydrogen, can emit a photon, leave the original magnetic field line, and get ionized again at some distance from the original travel direction. (From Egeland and Burke 2019)

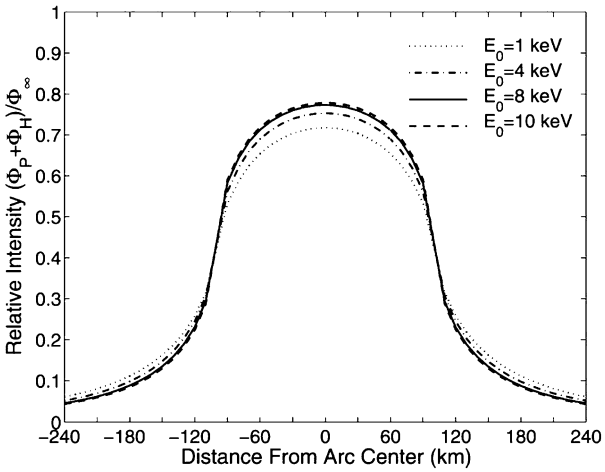


**Fig. 2** Relative intensity of the total downward H+ and H fluxes at 300 km altitude with respect to the homogeneous input at the top. The incident proton fluxes have a Maxwellian distribution with the characteristic energy of E0 = 1, 4, 8, and 10 keV. The semi-width of the proton arc is W = 100 km. (From Fang et al. 2004)

a substantial reduction of the background and a clear selection of red-shifted signal coming from protons with more than 1 keV energy (Mende et al. 2000). In the remainder of this paper we will use this second interpretation of the term "proton aurora" to clearly identify signal that can only originate from energetic proton precipitation.

The charge exchange and photon emission can generally be described as:

$$p^+ + X \quad \rightarrow H^* + X^- \quad \rightarrow H + h\nu + X^- \tag{1}$$

where $p^+$ is the energetic proton, X is an atmospheric constituent (mostly $N_2$ but also N, O, $O_2$), H* is the excited hydrogen atom, $X^-$ the ionized atmospheric constituent, H the hydrogen atom in its ground state, and $h\nu$ the hydrogen photon. The still energetic hydrogen atom can ionize again (Fig. 1) and continue as an energetic proton. The process repeats itself until the energetic proton achieves thermodynamic equilibrium with the surrounding medium. Additionally, the ionized constituent can emit auroral photons (for instance, the $N_2$

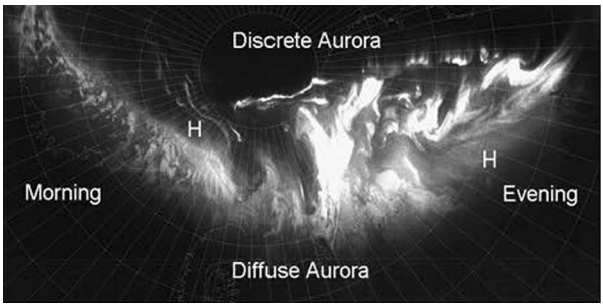


**Fig. 3** A synoptic image of nightside aurora showing the relative location of the hydrogen emissions – marked with H – versus the mostly electron generated oval, in both the morning (left) and evening (right). On the evening side the Balmer radiations are equatorward of the electron aurora, while on the morning side (left) the opposite is the case. (From Egeland and Burke 2019)

1st negative emission) which do not carry information about the generation partner and will generally be misidentified as "electron aurora".

First identifications of hydrogen Balmer lines were reported in the 1930/40 s (see Chamberlain 1961). Significant effort was then put into the identification of emission lines and the source of energetic protons (Egeland and Burke 2019). With improved ground instrumentation in the 1950/1960 s, particularly space-based particle detectors and imagers, the distribution and importance of proton precipitation in certain regions was recognized. One important difference between electron generated aurora and proton aurora is the reversal of the relative magnetic latitude distribution between both types of aurora (Fig. 3). Before magnetic midnight the proton aurora oval spreads equatorward, and peaks in intensity equatorward of the electron-generated green line. After magnetic midnight the hydrogen emissions are mainly observed poleward of the electron oval (i.e., MLat $> 70°$). However, the latitude distributions also depend on the energies of precipitating protons. Today proton aurora observations allow the assessment of the source region of energetic protons. They also can be used to identify the associated magnetospheric processes and to evaluate the ionospheric perturbations induced by energetic protons. The source regions include the cusp, the low-latitude boundary layer, the mantle, and the plasma sheet, including their dayside extensions (Galand and Chakrabarti 2006).

Secondary electrons produced within the proton beam contribute to "electron auroral" emissions. Since they are less energetic than the secondary electrons produced in electron aurora, they have a different spectral signature. In addition, for a given energy flux, protons are usually more efficient at ionizing than electrons and yield larger values of the Pedersen ionospheric conductance (Galand and Lummerzheim 2004). This difference between proton and electron aurora can lead to misinterpretation when brightness ratios are used to derive ionospheric conductances with parameterizations that are based on electron aurora. At the equatorward edge of the afternoon oval, where protons are a significant energy source, the traditional auroral analysis (Rees and Luckey 1974) using two lines to determine electron energy is limited. In regions of $>4$ keV electron precipitation, the presence of proton precipitation (even modest $\sim$10%), yields a large underestimation of both the electron mean energy and the energy flux. Overall, the presence of proton precipitation yields a poor estimation of the electron mean energy. In proton-dominated aurora, the Pedersen and Hall conductances are often underestimated. However, in location where the protons are not dominant and the electron precipitation is not too energetic, it is legitimate to estimate the particle characteristics and ionospheric conductances from the FUV brightnesses assuming pure electron

precipitation. This is true in particular for the region around midnight (1900–0400 MLT), at a magnetic latitude of 65–67° (Galand and Lummerzheim 2004).

The general view that proton aurora is located equatorward of electron aurora in the dusk-side of the auroral oval was later slightly modified as it was shown that the location depends on the level of geomagnetic activity (Zou et al. 2012). A statistical study of the absolute and relative locations of the equatorward boundaries of the proton and diffuse electron auroras used meridian scanning photometers to observe 630.0 nm emission from "electron aurora" and 486.1 nm ("H-$\beta$") emissions of proton aurora together with particle data from satellites. The statistical studies showed that the quiet time dusk-premidnight proton aurora extends slightly equatorward of the electron aurora. This is reversed on the dawnside. In contrast, the electron aurora during moderate and active intervals lies equatorward of the proton aurora throughout the nightside region (20–03 MLT). There is a dawn-dusk offset in the auroral oval location, with the proton aurora shifting toward premidnight and the electron aurora toward postmidnight. The penetration of the electron boundary equatorward of the proton precipitation across this MLT range had not been previously identified. Zou et al. (2012) attributed this to the fact that the equatorward part of the diffuse electron aurora is produced by lower energy electrons to which the 630.0 nm emission is more responsive and so marks a more realistic location of the electron equatorward boundary than do the 557.7 nm and UV emissions used in previous intercomparisons of these boundaries.

On the nightside, the bright proton aurora forms a band of diffuse aurora near the equatorward boundary of the electron auroral oval. Donovan et al. (2012) demonstrated that the precipitation is due to strong pitch angle diffusion that is thought to be the result of non-adiabatic motion of sub-keV to tens of keV central plasma sheet (CPS) protons as they traverse the tightly curved magnetic field topology in the vicinity of the neutral sheet. These authors also provided an overview of the relationship between the spatiotemporal evolution of the proton aurora and magnetospheric dynamics. They focused on the equatorward boundary of the proton aurora, the latitude of which has been shown to be strongly correlated with magnetic field line stretching in the inner CPS, and they provided the first-ever identification of the position of the ion isotropy boundary relative to equatorial magnetospheric spacecraft.

The bright proton aurora is generally understood to be the projection of the CPS onto the ionosphere. Particles in the CPS have sufficient particle energy to cause bright proton aurora luminosity after strong pitch angle scattering (presumably due to field line curvature). This region is often interpreted as the transition region between dipolar and tail-like magnetic topologies. Spanswick et al. (2017) presented statistics of proton aurora luminosity computed from THEMIS electrostatic analyzer measurements for various radial distances in the magnetotail. These results were compared to ground observations of proton auroral luminosity and used to derive a statistical source region of the bright proton aurora. They found that near magnetic midnight, the bright proton aurora rarely, if ever, maps to a location beyond 10 RE. They also showed that once inside of 6 RE, the predicted proton auroral luminosities become large relative to those typically observed. This likely indicates that 6 RE is typically inside of the ion scattering (isotropy) boundary. Spanswick et al. (2017) further asserted that this implies the bright proton aurora typically maps to the region between 6 RE and 10 RE in the tail.

Optical auroral measurements have repeatedly revealed the existence of a transitional stage between a quiescent preexisting arc and its significant auroral expansion in a substorm onset. Such a transitional stage of substorm onset (TSSO) is characterized by a gradual intensification and the emergence of auroral beads, along the preexisting arc. Prior studies on TSSO were limited to electron auroras which are dominant in optical luminosity. Liang

et al. (2018) used 12 substorm events to investigate the proton auroral features during the late growth phase and the TSSO. They confirm the previous notion that the onset electron auroral arc is usually located at the poleward "shoulder" of the main proton auroral band. Furthermore, while the electron auroral arc typically intensifies by a few times or even an order of magnitude during the TSSO, the concurrent proton aurora at the same location as the electron auroral arc shows much less noticeable variations. The proton auroral variations averaged over the arc band, as well as that integrated over the entire latitudinal range, are mostly within 10% of their mean late-growth-phase levels during the TSSO. Substantial intensifications of proton auroras occur after the poleward expansion of electron auroras. Even considering the spatial spreading of proton auroras, they estimated that the variation of ion precipitation fluxes on top of the ionosphere would be typically $<30\%$ during the TSSO. Liang et al. (2018) interpreted it as non-significant ion energization or large-scale magnetic field reconfiguration during the TSSO. Instead, it is likely that the underlying mechanism of the TSSO might be some instability wave mode. The instability wavelength is comparable to the ion gyroradius, so that the ions are demagnetized, suppressing ion flux variations with the instability. Enhancing upward electric fields in the auroral acceleration region during the TSSO may also play a partial role in weakening the ion precipitation flux variation.

## 3 Detached Subauroral Arcs

### 3.1 Afternoon Detached Auroral Arcs

Afternoon detached auroral arcs are equatorward to the main auroral oval, often connected to it near noon (Immel et al. 2002). Their properties and conditions are summarized in Table 1 of (Frey 2007). They occur in the general magnetic local time (MLT) region of 12–18 hours after a change of either the Interplanetary Magnetic Field (IMF) Bz or $B_y$ from negative to positive (Burch et al. 2002). Early after their discovery it was speculated that these arcs are "leftovers" of a preexisting arc when the auroral oval either contracted (Moshupi et al. 1979) or moved poleward in response to the $B_z$ or $B_y$ change, respectively (Burch et al. 2002). Early observations of detached arcs by the ISIS-2 photometers (Anger et al. 1978) detected only precipitating electrons, while later observations by IMAGE-FUV detected strong proton precipitation that could account for the entire "electron aurora" signal (Frey 2007). It is unclear if the electron and proton arcs are inherently different, or if the early photometers were not sensitive enough to detect the missing proton component. It should be noted that the positions of electron and ion precipitation boundaries in the dusk sector are nearly coincident for all levels of magnetic activity. However, the latitudinal distribution of energy fluxes indicates that the positions of electron and ion precipitation maxima are spatially separated. Maximum energy fluxes of ions are observed at the equatorial precipitation boundary, while those of electrons at the poleward one (Vorobjev and Yagodkina 2014).

Burch et al. (2002) suggested that detached afternoon arcs are generated by a well-established sequence of events. During stronger geomagnetic activity, which is often related to extended periods of southward IMF, ions are injected at the night side, drift around the dusk side towards the dayside, and precipitate into a proton arc along the equatorward part of the main afternoon auroral oval. That afternoon oval is mostly created by low energy electrons and has a general diffuse aurora appearance. A polarity change of the IMF Bz or $B_y$ causes a contraction and poleward motion of the diffuse auroral oval. However, the ring current proton precipitation remains unchanged and leaves the proton arc mostly unaffected; thus, the gap between the oval and the detached arc develops (Fig. 4).

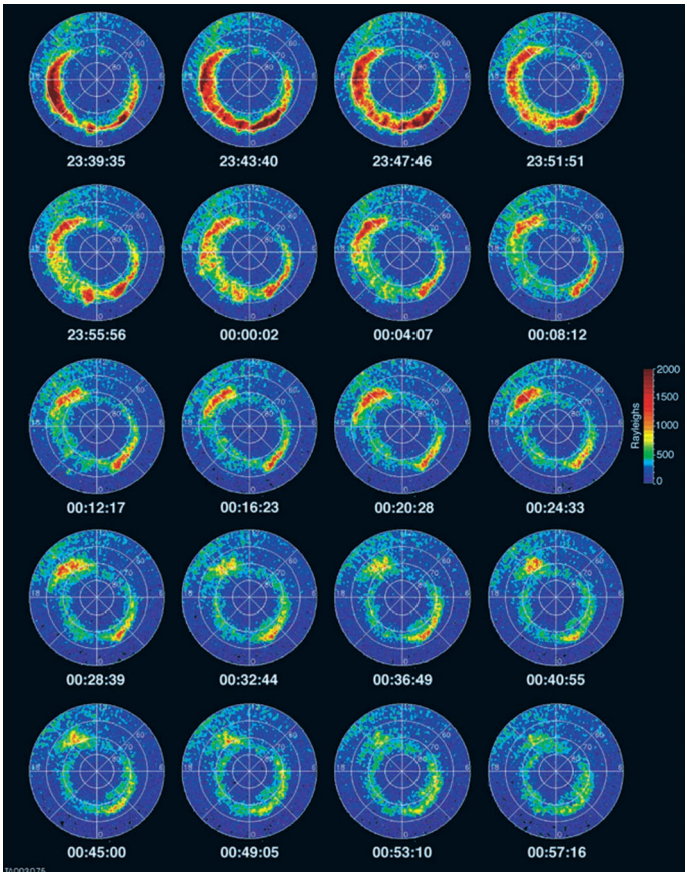


**Fig. 4** Proton aurora images on 9–10 November 2000 demonstrating the separation of a detached afternoon arc from the auroral oval after a strong magnetic storm and IMF rotation to northward direction. Times shown are in universal time. Pixels were mapped into geomagnetic latitude and local time coordinates. Noon is at the top. The false color indicates the emission intensity in Rayleighs. (From Burch et al. 2002)

Spasojevic et al. (2004) present a case study in which coincident observations of IMAGE in the far ultraviolet (FUV) and extreme ultraviolet (EUV) establish a causal relationship between a detached afternoon proton arc, and a plasmaspheric plume that extended from a contracted plasmasphere towards the dayside magnetopause. During a geomagnetic disturbance, the plasmasphere contracted and a distinct plume formed because of enhanced sunward convection and corotation flows across the dayside (Fig. 5). After a polarity change of Bz the convection decreased, and corotation dominated the flow inside the magnetosphere. This caused the plasmaspheric plume to further corotate into the afternoon sector where a detached proton arc had developed. Magnetic mapping using the IGRF plus Tsyganenko-96 magnetic field model (Tsyganenko 1995) established the magnetic connection between the two phenomena. It was early on speculated that the proton precipitation may be due to pitch angle scattering of energetic protons by electromagnetic ion cyclotron (EMIC) waves, which may be preferentially generated within the plume since the presence of cold, dense ions lowers the threshold for the EMIC instability (Spasojevic et al. 2005; Spasojevic and Fuselier 2009).

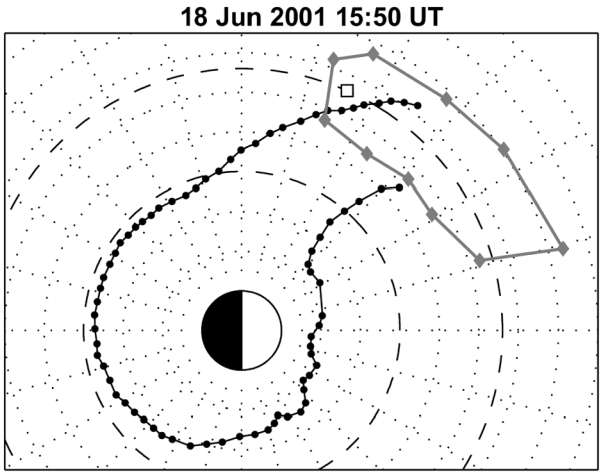


**Fig. 5** Contour plot of the plasmapause (black circles) and the mapped proton arc (gray diamonds) in the geomagnetic equatorial plane. The coincidence of both features creates the link between the plasmaspheric plume and the afternoon arc (reproduced from Spasojevic et al. 2004)

Electromagnetic ion cyclotron (EMIC) waves are generated in the equatorial region of the plasmasphere-magnetosphere by internal wave-particle interaction with ring current ions (Fraser et al. 2006; Ebihara and Khazanov 2016). In ground observations, they are observed as Pc 1-2 (0.1–5 Hz) waves, and one group of waves exhibits a spectral fine structure that has been classically explained by bouncing packet field-aligned propagation. An unstructured class of Pc 1-2 waves, including intervals of pulsations with diminishing period, lacks a fine structure pattern and is the dominant emission observed in the middle and outer magnetosphere by satellites. The cold/cool magnetospheric plasma has a profound effect on the generation and spectral properties of EMIC waves (de Soria-Santacruz et al. 2013). The waves are often observed at geostationary orbit within the outer magnetospheric extension of plasmaspheric plasma plumes as seen by the IMAGE spacecraft in the EUV imager instrument and are associated with subauroral proton arcs seen by the FUV imager. This provides evidence in support of a ring current loss mechanism induced by pitch angle scattering of protons by EMIC waves (Jordanova 2020). Characteristic frequencies introduced into the cold/cool plasma by heavy O+ and He+ ions determine the EMIC wave spectra, and these may be used in plasma diagnostic studies.

Jordanova et al. (2007), confirmed the connection between EMIC waves and afternoon detached arcs with calculations using a kinetic physics-based model coupled with a dynamic plasmasphere model. These authors calculated the growth rate of EMIC waves self-consistently with the evolving ring current H+, O+, and He+ ion distributions. The aforementioned study found that EMIC waves are preferentially excited, and proton precipitation maximizes, within regions of spatial overlap of energetic ring current protons and dayside plasmaspheric plumes and along steep density gradients at the plasmapause. The model matches very well the temporal and spatial evolution of FUV observations of the detached proton arc (Pierrard et al. 2009).

The connection between particle precipitation and EMIC waves was also seen on the ground as geomagnetic Pc1 pulsations and Intervals of Pulsations with Diminishing Periods (IPDP) (Yahnin and Yahnina 2007; Yahnin et al. 2009). Particle precipitation signatures of ion-cyclotron interaction were described from low-altitude satellite measurements of the energetic proton fluxes as well as from observations of the proton aurora. As a result, localized proton precipitation patterns were shown as an elongated region of the precipitation, presumably mapped onto the plasmaspheric plume. Clear evidence of the pitch-angle scattering associated with the ion-cyclotron wave activity was found near the equatorial plane

in the region conjugated with the localized proton precipitation at low altitude. Thus, the revealed precipitation patterns determined the location of the region of intense pitch-angle scattering of energetic protons. The proton arcs tend to appear at lower latitudes at later magnetic local times (MLTs). This agrees with the fact that the IPDP occurrence exhibits a similar behavior and that the IPDP end frequency tends to increase with increasing MLT (Yahnin et al. 2009). The spatial-temporal correlation of IPDP with proton aurora arcs confirms the expectation that the proton arcs are the ionospheric image of the region where the ion cyclotron instability develops in the equatorial magnetosphere. In the case of IPDP, the instability develops when drifting proton clouds resulting from particle injections in the night sector contact the plasmaspheric plume onto which the proton arcs map.

Ground-based observations of aurora and geomagnetic pulsations at subauroral latitude, using an all-sky imager and an induction magnetometer revealed isolated auroral arcs separated equatorward from the main auroral oval (Sakaguchi et al. 2008). The arcs were observed in both pre- and post-midnight sectors during the late recovery phase of geomagnetic storms. They found that as isolated arcs moved equatorward (poleward), the frequencies of the simultaneous Pc 1 pulsations increased (decreased). Using the Tsyganenko-02 magnetic field model (Tsyganenko 2002), the observed Pc 1 frequencies were almost the same as the frequencies of He+ EMIC waves at the equatorial plane connected to observed isolated arcs. These results also imply that the dynamics and instabilities in the inner magnetosphere can be monitored from the ground as low latitude auroral emissions away from the ordinary auroral oval.

The characteristics of precipitating ring current (RC) ions/electrons and precipitating radiation belt electrons associated with wave-particle interactions in the plasmaspheric plume in the main phase of a geomagnetic storm was investigated by Yuan et al. (2010, 2013). With observations of the NOAA-16 satellite, within the anisotropic zone, the peak of precipitating RC electron flux was equatorward to that of precipitating RC proton flux in a plasmaspheric plume recognized by the IMAGE and LANL-91/94 satellites. An enhancement of precipitating flux for $>3$ MeV electrons was simultaneously observed by NOAA-16 with the increase of precipitating RC proton flux within the anisotropic zone. Theoretical calculations of pitch angle diffusion coefficients for RC protons and for radiation belt electrons caused by EMIC waves demonstrated that precipitating flux enhancements of RC protons and $>3$ MeV radiation belt electrons are a result of EMIC wave-particle interactions in the plasmaspheric plume. These results suggest that EMIC waves in the plasmaspheric plume can scatter not only RC ions but also radiation belt electrons into the loss cone, thus explaining the existence of both proton and detached electron arcs.

### 3.2 Subauroral Spots

There are two types of subauroral spots, those with pure electron precipitation and those with pure proton precipitation. Their size is of the order of $\sim$100–300 km diameter, they can last for many hours, and they generally corotate with 70-95% of the full corotation speed. General properties and conditions are summarized by Frey (2007). The very first study of such patches in the evening region, coined Evening Corotating Patches (ECP), concluded that they are relatively rare, occur during weak geomagnetic activity, and are created by high-energy electrons (Moshupi et al. 1977). Their location and coincident plasma measurements led to the conclusion that they had to be created by particles originating at the plasmapause. The electron cyclotron wave resonance was suggested as a potential generation mechanism.

ECP also showed up in ground-based all-sky camera observations in many different wavelength bands (Kubota et al. 2003). The patches were clearly visible in emissions that

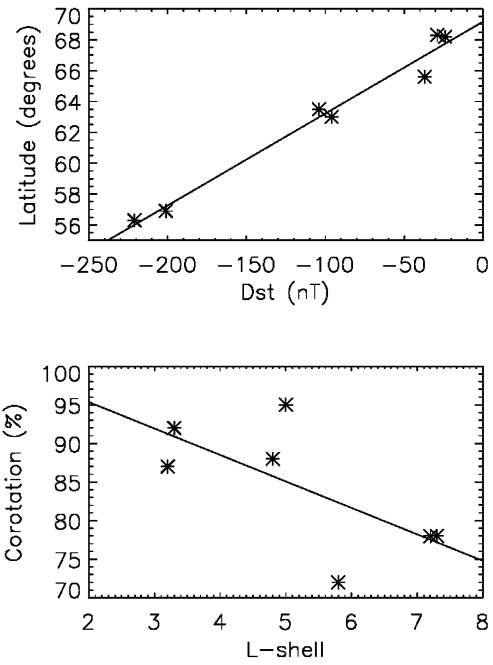


**Fig. 6** (Top) Relationship between the latitude of SAMPS observation and the minimum Dst of the previous geomagnetic storm. The correlation is 0.98. (Bottom) Relationship between the corotation speed of SAMPS and the L-shell of the location. The correlation coefficient is −0.68. (From Frey et al. 2004)

are generated by higher energy electrons, but they were absent in low-energy electron aurora and proton aurora. Simultaneous particle measurements by a low-altitude satellite confirmed the absence of proton precipitation, and the electron energy was greater than 10 keV. Earlier observations from a different study placed the patches at plasmapause latitude (Moshupi et al. 1979). The interaction of cold plasmaspheric plasma at plasmapause undulations with drifting higher energy electrons, could account for the scattering of electrons into the loss cone and cause their precipitation into the ionosphere (Krall and Huba 2016).

The second category of subauroral spots created by pure proton precipitation was first described as Subauroral Morning Proton Spots (SAMPS), which were seen in the proton aurora channel of the IMAGE-FUV Spectrographic Imager (Frey et al. 2004). In the aforementioned study, SAMPS were observed in the Wideband Imaging Camera that is primarily sensitive to emissions from electron precipitation; however, energetic protons will also excite higher energy levels of atmospheric constituents ($N_2$ and O) that will then appear as electron aurora. Two passes of low-altitude spacecraft through the same flux tubes confirmed the pure proton precipitation and the lack of higher energy electrons.

The long observational periods from the high-altitude IMAGE orbit together with the long-lasting duration of these spots allowed for a detailed investigation into their occurrence and their dynamics. Frey et al. (2004) found subauroral spots to appear in the recovery phase of geomagnetic storms. The spots could be seen for several hours moving towards later local times with a little bit of lack behind true corotation speed. Different spots appeared at different geomagnetic latitudes. The authors found a good relationship between the minimum Dst of the prior geomagnetic storm, together with a strong relationship between their geomagnetic latitude (or L-shell) and their corotation speed (Fig. 6).

Coincident observations of the plasmasphere by IMAGE-EUV confirmed the relationship between SAMPS spots and spatial modulations of the plasmapause in two instances. In these two cases, the auroral spots magnetically mapped once to a notch and once to a shoulder in

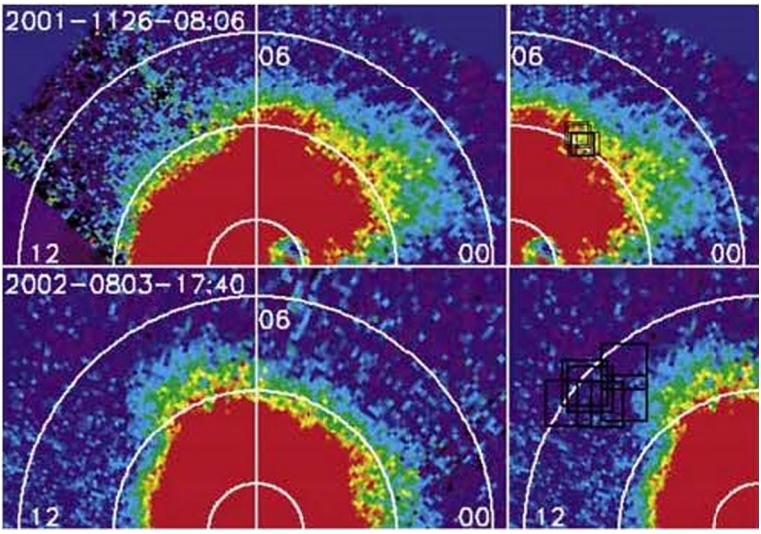


**Fig. 7** (Top) EUV image of the plasmasphere at 08:06 on 26 November 2001, as mapped to the geomagnetic equator. The dynamic range was exaggerated to show the notch in the plasmapause at L = 3 and MLT = 4 hours. The left part shows the EUV image with the noon meridian to the left. The right part shows the location of SAMPS at ±5 min around the EUV center time mapped to the magnetic equatorial plane. (Bottom) The same for 3 August 2002 at 1740 UT when SAMPS were observed around 1000 MLT. The size of the squares in the two right panels represents the diameter of the magnetic flux tubes originating in the spots with the larger area for flux tubes originating at higher latitude and mapping to larger distances. (From Frey et al. 2004)

the plasmapause. Figure 7 shows these two cases with the SAMPS locations mapped into the EUV images. The speeds of the spot and the plasmaspheric shoulder were 88% and 94% of the corotation speed, respectively.

The above mentioned connection between the locations of spots and of modulations in the plasmapause suggested that wave-particle interactions can cause the precipitation of energetic protons. After strong geomagnetic storms, the originally eroded plasmasphere expands again. The cold plasma corotates and interacts with enhanced fluxes of trapped ring current ions. The energy limit for the interaction between ring current ions and EMIC waves is lowered, allowing a larger portion of the ion distribution function to be scattered into the loss cone.

The hypothesis that this proton aurora is produced by energetic proton precipitation after the interaction of ring current particles with electromagnetic ion cyclotron (EMIC) waves in the equatorial plane of the magnetosphere was further confirmed by ground-based observations of Pc1 pulsations (Yahnin et al. 2007). Geomagnetic pulsations Pc1, which are a ground signature of EMIC waves, were found when the proton spot is nearly conjugated with the ground station equipped with a pulsation magnetometer. Moreover, there is a good agreement between the appearance/disappearance of the spot and the beginning/end of the Pc1 train. Thus, the subauroral proton spots are images on the ionospheric "screen" of magnetospheric regions where the ion cyclotron instability develops leading to an intense scattering of energetic protons into the loss cone.

Proton aurora patches similar to SAMPS were also observed in the same evening local time region as the ECP (Zhang et al. 2005). However, simultaneous low altitude satellite particle measurements exhibited the absence of any electron precipitation and showed

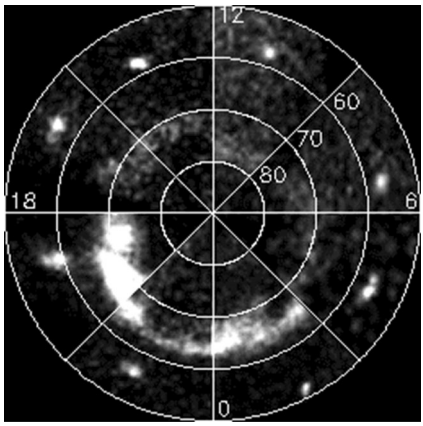


**Fig. 8** Collage of "pie-sections" from eight different original images by IMAGE-SI demonstrating the occurrence of localized proton spots at all local times. The eight original raw images were collected on different dates in 2000–2002

pure proton spectra with average energies of 10–20 keV. Evening proton spots appeared at lower magnetic latitude of 45°–55° during the main phase of strong storms, while the electron spots generally appeared at higher latitude of 58°–65° after minor to moderate storms (Moshupi et al. 1979). This difference may not be important as bigger storms erode the plasmasphere stronger, but it is still unclear what causes in one case the wave-particle interaction of EMIC to scatter ions, and in other cases the electron cyclotron waves to scatter electrons. Are different processes responsible for the ion and electron scattering, or are there just two aspects of the same process at work? Observations by the IMAGE Spectrographic Imager (Mende et al. 2000) revealed more cases of pure proton spots occuring at all local times and not just in the morning and evening (Fig. 8).

In a later study, Sakaguchi et al. (2012) presented ground-based observations using all-sky imager and search coil magnetometer networks, which provide the large-scale distribution and motion of the EMIC wave-particle interaction regions. They observed several spots of isolated proton auroras coincident with Pc1/EMIC waves at subauroral latitudes during the expansion phase of a storm-time substorm. The isolated auroras were distributed over 4-hours MLT preceding midnight. The POES-17 satellite confirmed enhancements of 30-keV proton precipitation over the isolated auroras. The equatorward motion of the auroras and frequency drift of the wave were consistent with the plasmasphere eroding due to a polar cap potential enhancement modeled by a numerical simulation (Sakaguchi et al. 2016). Similar results were reported by Søraas et al. (2013) who determined proton energies of up to 100 keV going into a proton spot, which mapped to the equatorial plasmapause.

Observational evidence of rapid luminous modulation of isolated proton aurora (IPA) spots correlated with Pc1 waves simultaneously observed from the ground, which are equivalent to the electromagnetic ion cyclotron (EMIC) waves in the magnetosphere as reported by Ozaki et al. (2018). The fastest luminous modulation of IPA was observed in the 1 Hz frequency range, which was twice the frequency of the related Pc1 waves. The time lag between variations of Pc1 wave power and the IPA luminosity suggests that the source regions of IPA are distributed near the magnetic equator, suggesting an EMIC wave-energetic (a few tens of keV) proton or relativistic (MeV or sub-MeV) electron interaction. The generation mechanism of this 1 Hz luminous modulation remains an open issue.

Yahnin et al. (2013) compared the projection of "proton aurora spots" with the location of the plasmapause. Their plasmapause formation model is based on the quasi-interchange instability mechanism and was used to determine the plasmapause location. This comparison showed that often the proton aurora spot source is located near the plasmapause location or

in the cold plasma gradient region just inside the plasmapause. In some events, the proton aurora spots mapped well outside the plasmapause. They suggested that in the latter case the ion cyclotron instability develops when westward drifting energetic protons interact with cold plasma that was earlier detached from the plasmasphere.

In a different study, two Pc1 bands were registered in the event when two proton auroral spots were simultaneously observed at different latitudes (Yahnina and Yahnin 2012). In this case, the Pc1 intensity distribution maximum at lower frequencies was related to a proton auroral spot at a higher latitude and vice versa. Such a spatial correlation between Pc1 pulsations and proton auroral spots, together with the previously established time correlation between these phenomena, demonstrates that subauroral proton spots delineate the region of ion cyclotron instability in the equatorial magnetosphere at the level of the ionosphere.

The relationship between evening corotating patches and processes in the plasmasphere and ring current were recently investigated through aurora and simultaneous particle observations by DMSP/SSUSI (Yao et al. 2019). The patches corotated with the Earth and stayed at a constant magnetic latitude. The particle measurements confirmed that energetic protons with energies above 20 keV without any significant electron contribution were responsible for the patches. The authors argued that the energetic ions producing ECP originate from the ring current, which is assumed to be filled with hot ions during the recovery phase of magnetic storms.

## 4 Stable Auroral Red (SAR) Arcs

In addition to the bright and variable optical emissions observed in the auroral oval, another zone of visible Magnetosphere-Ionosphere (M-I) coupling is the sub-auroral ionosphere-thermosphere system. Here, one of the optical structures typically observed is known as a SAR (Stable Auroral Red) arc. Its location and occurrence are directly linked to the ionospheric trough/plasmapause region– a region of reduced electron density. The poleward wall of the trough is caused by ionospheric plasma produced by the precipitation of low energy ions and electrons. The equatorward wall of the trough is the gradient caused by normal post-sunset decay ionospheric plasma. During geomagnetic quiet times, the trough is at approximately 60° magnetic latitude. This corresponds to an L shell value of 4, with L being the distance at the magnetic equator measured in Earth's radii. The magnetospheric region interior to this boundary is the *plasmasphere*—a region filled by upward flowing cold ionospheric plasma. Within the magnetosphere, this important field-line boundary is called the *plasmapause*, and it corresponds, approximately, to the separation of co-rotating plasma from plasma undergoing magnetospheric convection. During geomagnetic storms the ionospheric trough and the plasmapause move to lower latitudes—most often to about $L = 3$. Auroral features are enhanced and the whole auroral oval moves equatorward. The SAR arcs intensify and can be observed at $L = 3$. Figure 9 shows a schematic representation of the inner magnetosphere adapted from Kozyra et al. (1987). The two rings labeled 'Conjugate SAR Arcs' are the ionospheric foot-points of the overlapping plasmasphere and ring current regions. A SAR arc is almost always subvisual, typically 10–20 times fainter than visible aurora. Initial observations showed that brightness levels remain virtually constant for hours, the emission was described as "spectrally pure" red (630.0 nm-only photons) from atomic oxygen excited to the $^1$D ($\sim$2 eV) state by ambient ionospheric electrons with $T_e > 3000$ K, and was a narrow emission feature (50–200 km) in N-S width, but with great E-W extent (1000's km) (Kozyra et al. 1997). This increased electron temperature is produced by heat

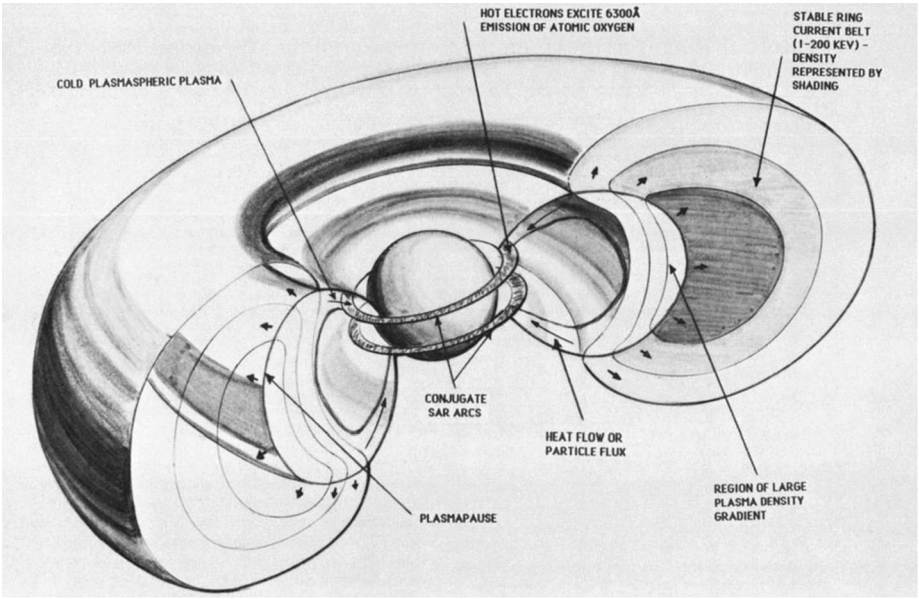


**Fig. 9** Schematic representation of the inner magnetosphere showing the overlap between the ring current and the plasmasphere. SAR arc emissions occur at the foot of the field lines that thread this overlapping region (Kozyra et al. 1987)

conduction or low energy precipitating electron flux from the ring current (Rees and Roble 1975).

Using 10 years of SAR arc intensities measured by a network of scanning photometers during 1978–1988, Lobzin and Pavlov (1999) presented a statistical study correlating these observations with different solar and geomagnetic activity indices. They showed that the electron temperature in the SAR arc region does not strongly depend on the electron density and is strongly coupled to the additional heating of the electron gas due to interaction of the ring current ions and plasmaspheric electrons. As a result, variations of electron temperature in the SAR arc region with characteristic time scales from several minutes to several hours could be a manifestation of time variations of ring current parameters.

Takagi et al. (2018) performed a statistical analysis of SAR arc detachments from the main oval based on 11 years of all-sky camera observations obtained at subauroral latitudes (at Athabasca, $L = 4.3$). The authors showed that the yearly variation of SAR arc detachments has a better correlation with the geomagnetic Ap index than the solar F10.7 index. SAR arcs tend to occur pre-midnight, and at the beginning of a substorm recovery phase. They concluded that the SAR arcs detach from the main oval as the main auroral oval returns to higher latitudes at the beginning of the recovery phase. An average SYM-H index of $\sim -20$ nT was observed, indicating that the observed detachments could be related to weak geomagnetic storm conditions or non-storm time substorms.

Seasonal studies have been described by several groups using ground-based data from a northern hemisphere site (Fok et al. 1993; Kozyra et al. 1997). Thus, the seasonal patterns they addressed were acquired sequentially and, during different geomagnetic storms. Their statistical findings were that emission levels were lowest in summer months. Only recently, SAR arcs were observed simultaneously in both hemispheres and their characteristics were investigated (Martinis et al. 2019; Hong et al. 2020).

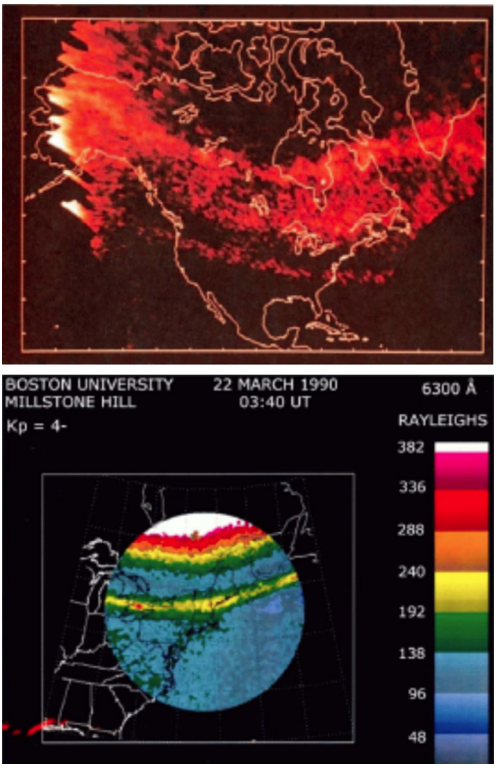


**Fig. 10** (Top) Dynamic Explorer 2 satellite observations of the northern hemisphere showing the red aurora at higher latitudes and a relatively thin arc equatorward it. This thin arc represents a SAR arc. (bottom) Ground-based all-sky image from Millstone Hill Imager showing a bright auroral display and a uniform east-west elongated arc at subauroral latitudes (adapted from Mendillo et al. 2013)

The following sections summarize past and present observations of SAR arcs, energy sources for their formation, and examples of SAR arcs that diverge from their classical definition.

### 4.1 Observations: Past and Present

The first observations of a SAR arc from space occurred with the Dynamic Explorer (DE) polar orbiting spacecraft. Figure 10 (top) shows a SAR arc over North America. The arc is the southernmost band of emission separated from the more northerly aurora (Craven et al. 1982).

Optical ground-based observations of SAR arcs were performed using scanning photometers and all-sky imagers. Figure 10 (bottom) shows a SAR arc, equatorward from the diffuse aurora, observed with the Millstone Hill all-sky imager (Mendillo et al. 2013). A relatively uniform and stable structure was typically observed. Radar measurements have revealed characteristic ionospheric parameters such as electron temperature (Te) and electron density (Ne) within a SAR arc. Figure 11 (left) shows results from the Millstone Hill incoherent scatter radar. Near 44° magnetic latitude decreased Ne and elevated Te in the altitude range from ∼300 to ∼600 km were measured. In addition, a strong westward drift was observed, consistent with a SubAuroral polarization stream (SAPS) co-located with a SAR arc (Spiro et al. 1979; Foster and Burke 2002). These results indicate that SAR arcs and SAPS might be related phenomena occurring simultaneously.

Previous studies have reported in-situ satellite observations of SAR arcs and SAPS, i.e., increased Te, decreased Ne, and elevated westward plasma flow (Rees and Roble 1975;

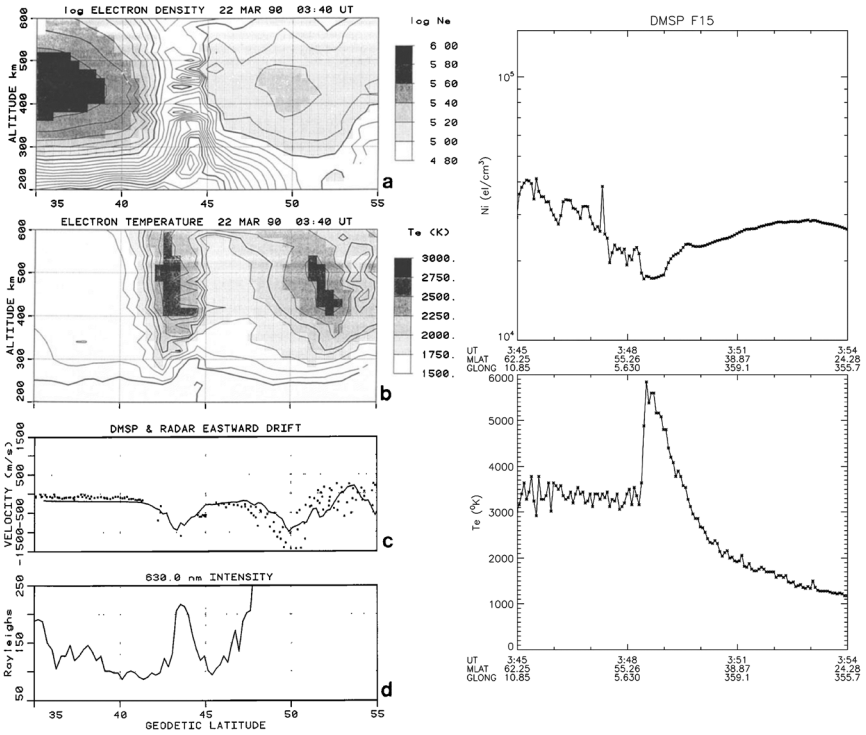


**Fig. 11** (Left) From top to bottom: (**a**) electron density height profile using the Millstone Hill ISR; (**b**) electron temperature, showing enhanced values near 43°; (**c**) Westward plasma flows obtained from radar and DMSP data; (**d**) 630.00 nm brightness showing a SAR arc (from Foster et al. 1994). (Right) DMSP F15 data showing ion density (top) and electron temperature Te (bottom). SAR arc signatures are visible as the spike in Te associated with a minimum in ion density (adapted from Mendillo et al. 2016a)

Kozyra et al. 1997). For example, Fig. 11 (right) shows data from DMSP, orbiting at ∼840 km, during the geomagnetic storm of 12 September 2013. The left panel shows Ne and Te measurements (a, b) and drifts (c) from Millstone Hill ISR. Airglow intensity from a collocated all-sky imager (ASI) is shown at the bottom (d). These plots clearly show the reduced Ne (a), increased Te (b), and westward SAPS flow enhancement (c) collocated with the higher brightness below 45° latitude indicating the presence of a SAR arc (d).

Evidence of wide longitudinal occurrence and long lifetime was reported by the DE-1 spacecraft when a SAR arc was observed in four subsequent, consecutive orbits spanning 28 hours (Craven et al. 1982). Recent observations (Mendillo et al. 2013) using multiple ground-based all-sky imagers have shown that SAR arcs extend along the entire globe, as depicted in Fig. 9. Three ASIs, located in North America, Europe and New Zealand detected a SAR arc during the 27 September 2011 storm as shown in Fig. 12. This study represents the first time that the same SAR arc has been seen from ground-based images from multiple continents in both hemispheres. The center of the SAR arc in each image was determined along the N-S meridian to create the local time versus latitude pattern for that night. Those locations were then mapped to the magnetospheric equatorial plane and their positions versus Local Time (LT) and L value appear at the bottom of Fig. 12. There is a clear trend of the SAR arc/plasmapause moving earthward from dusk to dawn (O'Brien and Moldwin 2003), similar to the morphology observed in SAPS (Foster and Vo 2002). To merge the

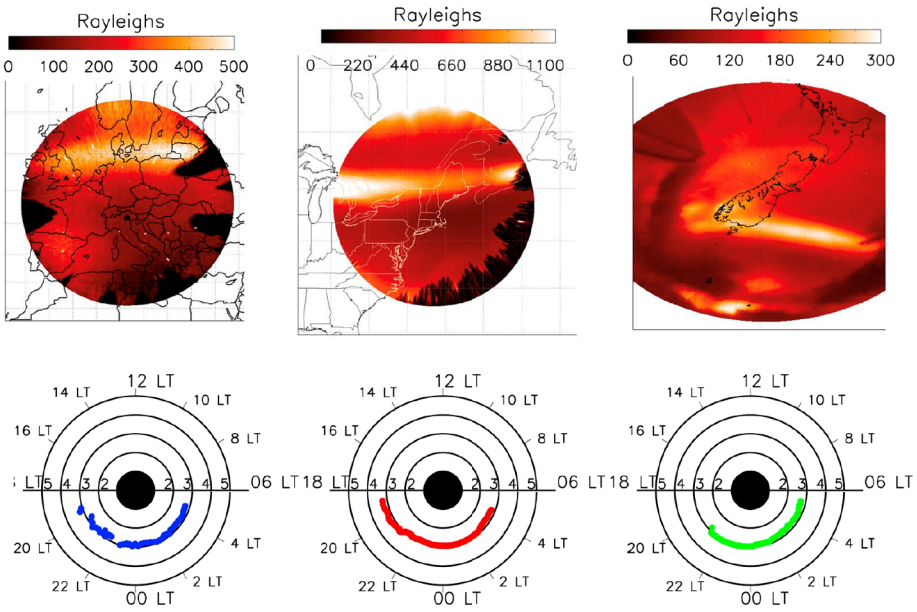


**Fig. 12** (Top) Sample images of a SAR arc at Asiago, Millstone Hill, and Mount John during the storm of 26–27 September 2011. (Bottom) Equatorial plane representation of the location of the arc (adapted from Mendillo et al. 2013)

three-site LT observations into a single composite result, the positions from each station were re-mapped into a UT and L value format (Fig. 13). The total data set spans darkness over ∼24 h of UT storm time. When the end of coverage at one station overlaps the onset of coverage at the next station, the dusk-dawn asymmetry in plasmapause location can be seen at specific UT periods. The clearest example of this occurs between 08:00 and 10:00 UT on 27 September when the dusk plasmapause is at $L = 3$ (from Mount John data) while the dawn plasmapause is at $L = 2.7$ (from Millstone Hill data).

Magnetically Conjugate observations of SAR arcs using satellite data have been reported by Reed and Blamont (1974) and LaValle and Elliott (1972). The Reed and Blamont's study was a brief report on the SAR arc of 28–30 September 1967 observed by the photometer onboard the Ogo-4 spacecraft. The Ogo-4 data in the southern hemisphere located the SAR arc within a few tenths of the L-value recorded in Idaho ($L \sim 3$). LaValle and Elliott (1972) analyzed three SAR arcs from the satellite OV1-10 that was launched in 1966 in a polar orbit. One of the SAR arcs was observed as a conjugate phenomenon on 16 February 1967. Brightness values did not differ much in both hemispheres: ∼ 500 R in the northern hemisphere as compared with ∼ 650 R in the southern hemisphere. Ground based studies in both hemispheres were presented by Roach and Roach (1963). They reported SAR arc observations in North America and in New Zealand, but at different times, i.e., not simultaneous conjugate observations.

SAR arc studies using two ground-based data sets linked by the same geomagnetic field line, i.e., *conjugate-point studies*, allow seasonal patterns and other hemispheric characteristics to be obtained *simultaneously*, not sequentially, as presented above. Martinis et al. (2019) showed results from two magnetic conjugate stations, Millstone Hill (USA) and Rothera (Antarctica), that are part of a network of all-sky imagers built and operated worldwide by Boston University (Martinis et al. 2018). Previous works addressing 'seasonal

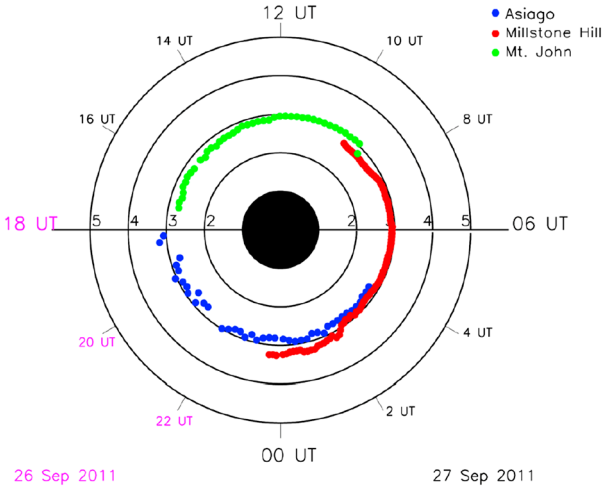


**Fig. 13** Location of the SAR arc of 26–27 September 2001 in UT obtained by merging the data from the local time patterns in Fig. 12. (From Mendillo et al. 2013)

asymmetries' relied on measurements at a single site during different seasons (implying different background conditions) and different storm conditions. The work by Martinis et al. (2019) showed for the first time simultaneous inter-hemispheric characteristics of SAR arcs during the 1 June 2013 geomagnetic storm.

Figure 14 shows unwrapped all-sky images at Millstone Hill (top) and the corresponding Rothera images (bottom). The circle in each image represents the zenith location and the asterisk indicates the conjugate location of the imager in the opposite hemisphere. The arcs are observed at the same magnetic latitudes in both hemispheres, i.e., they are magnetically conjugate. The middle panel shows the arc overhead at Millstone Hill and the arc observed at Rothera falls right on top of the conjugate location of Millstone Hill. Both arcs seem to have similar width, although one of the main differences is that the poleward edge of the arc at Rothera is sharper and less diffuse than the one observed at Millstone Hill. This effect is not related to viewing geometry or differences in the two optical systems. Figure 15 shows brightness values (background subtracted) for the SAR arcs at Millstone Hill and Rothera for all the images taken on 1 June 2013. The ∼30-minute data gap in the Rothera curve represents a brief period when clouds affected the calibration at this site. A ±25% uncertainty in brightness is shown in each data point. The SAR arc at Rothera is clearly brighter than the one observed at Millstone Hill, at times by a factor of 2–3. Both arcs show simultaneous brightness variations during the night. Martinis et al. (2019) argued that the observed changes were related to changes in solar wind/magnetospheric activity, as measured by different solar wind parameters, geomagnetic indices and particle flux data. The main conclusions in the study showed that: (a) the SAR arc observed at one site is seen at its magnetically conjugate location; (b) the SAR arc at Rothera (winter) is brighter than the one observed at Millstone Hill (summer), sometimes by a factor of 2–3 and similar changes in brightness are observed at both sites throughout the night; (c) both arcs show the same equatorward motion and have similar latitudinal width, although the poleward edges of the arcs at Rothera are sharper.

A recent study by Hong et al. (2020) used the Millstone Hill ASI and a conjugate ASI at the King Sejong Station, close to the Rothera ASI, to compare SAR arcs during the St. Patrick's Day storm in 2015. They determined that ionospheric irregularities occurred only near the diffuse aurora and not in the SAR arc and found that the Millstone Hill arc showed a broader latitudinal extent.

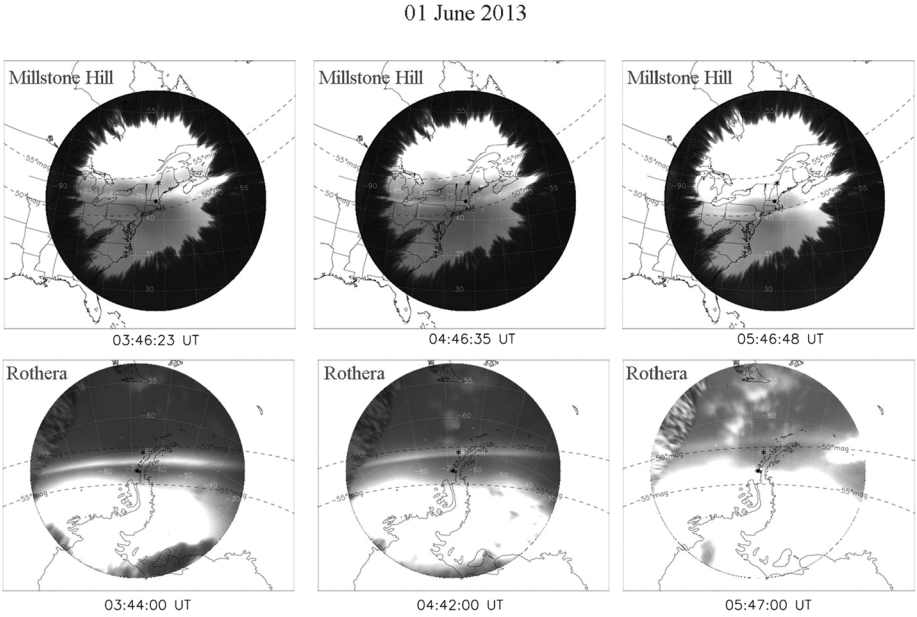


**Fig. 14** (Top) Simultaneous images from Millstone Hill all-sky imager (ASI) and (bottom) Rothera ASI at three different times. The black circles indicate the zenith location and asterisks show their respective conjugate points. (From Martinis et al. 2019)

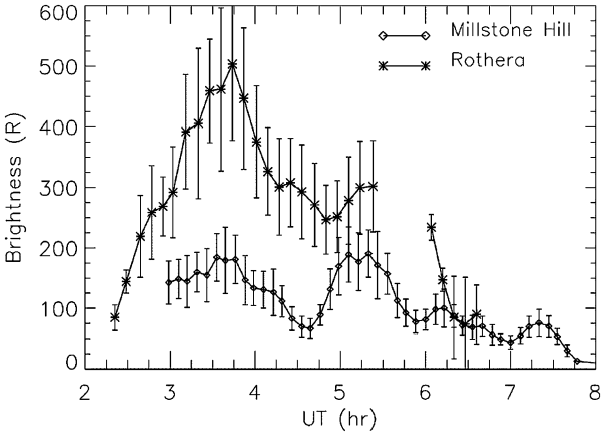


**Fig. 15** (Millstone Hill (diamonds) and Rothera (asterisk) SAR arc brightness (above background airglow levels). The SAR arcs curves at both sites follow a similar trend, with Rothera values being larger than Millstone Hill values. Error bars represent the uncertainty in the determination of the brightness values. (From Martinis et al. 2019)

## 4.2 Energy Source of SAR Arcs

There are no conclusive observations or theories explaining how the energy required to feed SAR arcs is generated. All the candidate energy source mechanisms require that a fraction of storm energy be transported from the inner magnetosphere (at $L \sim 3$) along magnetic field lines down to F-region heights via heat conduction or soft electron precipitation (Rees and Roble 1975). According to Fok et al. (1991, 1993), this heat conduction is understood as the downward transport (into the ionosphere along field-lines) of energy produced by the interaction of energetic ring current ions with plasmaspheric electrons.

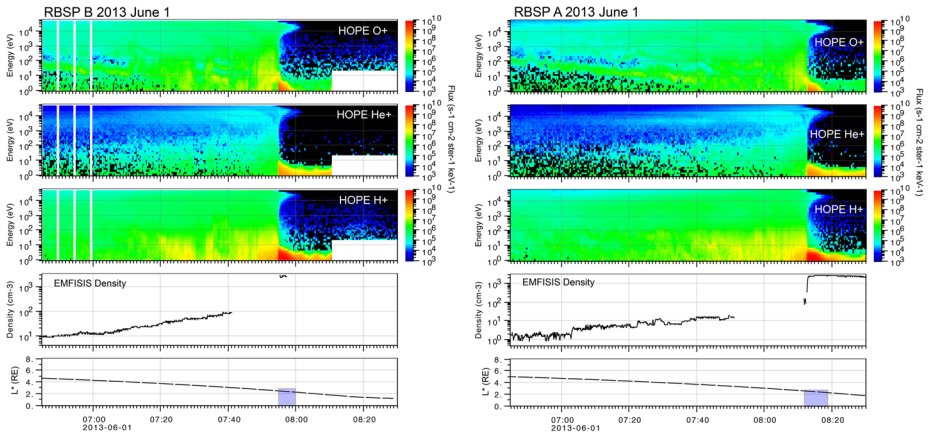


**Fig. 16** HOPE and EMFSIS data for VAP B (left) and VAP A (right). The location of the plasmapause coincides with the increase in fluxes in the three ion species between ∼08:00UT and 08:20UT. Both probes sample the field lines that connect to the subauroral ionosphere where a SAR arc is being measured by the Millstone Hill ASI (Showed as the shaded blue region)

Cole (1965) described the connection between SAR arc emissions and collisional interaction between ring current ions and electrons in the plasmasphere. The amount of energy transferred to the thermal electrons is a function of the temperature and density of the plasmaspheric thermal electrons and the magnitude, composition and energy distribution of the ring current. Using satellite data and ground-based scanning photometers Kozyra et al. (1993) explained the occurrence of SAR arcs during the different phases of a storm. For SAR arcs occurring during the recovery phase, it was observed that $O^+$ was the dominant energy source for SAR arcs; while during the main phase of the storm, medium energy $H^+$ was significantly enhanced. Column electron heating rates were computed using a well-established model (Rees and Roble 1975) that takes into account the flux and energy of ring current ions and their interaction with plasmaspheric thermal electrons at a given temperature and density. Calculations show that the maximum energy losses depend on the interaction between ring current ions of particular energy ranges with thermal plasmaspheric electron populations. For a SAR arc's typical electron density (Ne) and temperature (Te), the peak in energy loss for $H^+$ and $He^+$ occurs at $E < 10$ keV, and for $O^+$ it occurs between 30 keV and 50 keV. These average maximum energy loss rates are shifted toward lower energy ions if the plasmaspheric Ne and Te are smaller (Kozyra et al. 1993). Modelling results show that after the interaction between the high energy ions and the plasmaspheric population an enhanced flux of very low energy ions (∼10's eV) is observed (Fok et al. 1993).

Ongoing studies are combining Van Allen Probes data with ground-based all-sky imagers detecting SAR arcs, trying to find out if these eV ion populations are observed near L-shell magnetic lines connecting with the sub-auroral ionosphere. Low energy ions measured by the Helium, Oxygen, Proton, and Electron (HOPE) instrument have been observed to increase near the magnetic equator on magnetic field lines that connect to locations where SAR arcs are observed. In Fig. 16 we show low-energy ion fluxes measured by HOPE, as well as cold density profiles derived from upper hybrid wave measurements provided by the Electric and Magnetic Field Instrument Suite and Integrated Science (EMFISIS). The blue-shaded regions mark the mapped locations of the ground-based observed SAR arc, for each probe (B is leading A). It can be seen that the arc maps to the plasmapause region and coincides with enhanced low energy ion fluxes. Figure 17 shows pitch-angle information

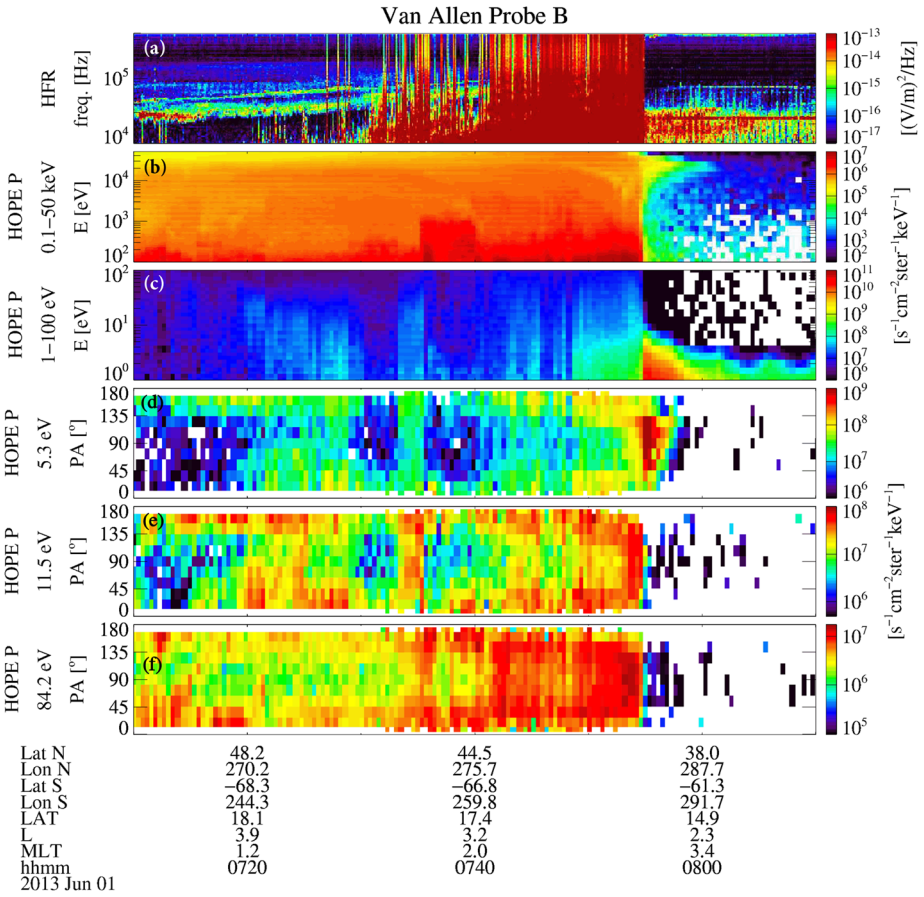


**Fig. 17** The $H^+$ ion distributions observed by Van Allen Probe B. (**a**) The high frequency wave electric spectrogram observed by HFR instrument; the energy spectrograms of spin-averaged proton fluxes observed by HOPE at energies (**b**) from 500 eV to 50 keV and (**c**) from 1 eV to 100 eV; the pitch angle spectrograms of proton fluxes observed by HOPE at energies of (**d**) 5.3 eV, (**e**) 11.5 eV, and (**f**) 84.2 eV. The spacecraft travelled from the plasma trough to the plasmasphere at ∼07:49 UT. The pitch angle distribution of protons evolved from mostly field-aligned to pancake-like during the plasmapause crossing, indicated by the appearance of trapped protons during ∼07:40–08:00 UT

for $H^+$ ions at several energies. When VAP-B crosses the magnetic field lines linked to the SAR arc predominantly trapped particles were observed, i.e., no evidence of ion outflows, as shown in the 11.5 eV and 82.4 eV panels between ∼07:30 and 08:00 UT. We also looked at the wave data for this event. During 07:30–8:00 UT, the EMFISIS data (not shown) indicate that no EMIC (electromagnetic ion cyclotron) waves were detected by either VAP A or B. VAP EFW (electric fields and waves) data published by Thaller et al. (2015) indicate persistent SAPS presence in the magnetosphere during this period.

Other generation mechanisms include interactions between thermal electrons and low frequency EMIC waves (Cornwall et al. 1971) and Landau damping of kinetic Alfven waves (Hasegawa and Mima 1978). Direct observations of ion cyclotron waves in the SAR arc region ($L < 4$) are not common. Anderson et al. (1992) studied the Pc 1-2 waves (0.1–4 Hz) in the L shell range 3.5–9 near the equatorial plane. They found that for L< 5 Pc 1-2 waves

occurred 1–2% of the time, while this percentage increased to 10–20% on the dayside at $L > 7$. This result was also obtained with the CRRES satellite. Iyemori et al. (1994) studied the relationship between Te enhancements in the sub-auroral ionosphere and Pc 1 waves measured near the plasmapause using DE 2 spacecraft. After examining thousands of orbits, only 22 events with large amplitude waves were found. Some of these events were accompanied by Te enhancements. Lanzerotti et al. (1978) examined two intervals of irregular magnetic activity during SAR arc observations on December 17–18, 1971. By assuming a wave amplitude of 10 nT the authors concluded that it was plausible that sufficient wave energy might be available to produce the SAR arc. Kozyra et al. (1987) showed a case where intense ELF hiss was observed at a field line in the magnetosphere that connected to an optically observed SAR arc. Recently, Wang et al. (2019) performed test-particle simulations at $L = 5$ to demonstrate the possible cold (1–10 eV) electron heating by EMIC waves with wave amplitudes of a few nT through nonlinear Landau resonance. The importance of plasma waves in SAR arc formation still remains poorly understood.

The role of large perpendicular electric fields in the ionosphere on the formation of SAR arcs has also been considered. At sub-auroral latitudes in the F-region it is fairly common to observe east-west elongated structures characterized by large northward electric fields of up to ∼100 mV/m, or a few mV/m in the equatorial plane, confined to narrow bands inside the main ionospheric trough in the evening local time sector. Depending on their characteristics they can be SubAuroral Polarization Stream (SAPS) (Foster and Burke 2002; Foster and Vo 2002; Clausen et al. 2012), SubAuroral Ion Drift (SAID) (Spiro et al. 1979; Mishin 2013), or Polarization Jet (PJ) structures (Galperin 2002). Sazykin et al. (2002) suggested that the presence of strong localized SAPS-like electric fields is potentially capable of powering weak (∼100 Rayleigh) SAR arcs. SAID events are supersonic westward plasma drifts on the equatorward edge of the diffuse aurora in the evening and nighttime sector. Their optical F-region signatures are weak 630.0 nm red arcs collocated with regions of fast convection. These weak arcs resemble SAR arcs observed during the recovery phase of magnetic storms, but have lower intensities, shorter lifetimes, and occur without a significant heat flux from the magnetosphere. Ion-neutral collisional heating and ion composition changes during PJ events may be an additional source of 630.0 nm emission. Ion-neutral frictional heating in the F-region may be capable of providing energy enough to excite weak emissions even without the heat flux from the magnetosphere postulated as the source of SAR arcs. As a test to distinguish PJ-related SAR arcs from ring current-induced arcs, Sazykin et al. (2002) suggested that some enhancement of the highly forbidden 5200 NI spectral line is expected in PJ-related arcs due to optical relaxation of $N(^2D)$.

It is possible that more than one mechanism is playing a role in the generation of energy to feed a SAR arc. For example, Jordanova et al. (1999) considered interactions between ring current protons and EMIC waves of the $He^+$ wave branch. The maximum wave gain occurred in the post-noon to midnight local time sector, just inside the plasmapause. Landau damping of these waves could represent an additional heat source for the elevated electron temperature observed at F region heights during the storm period. Total magnetospheric heating, resulting from both Coulomb collisions and wave-particle interactions will thus maximize near dusk, in agreement with previously reported westward intensifications of SAR arcs emission (Kozyra et al. 1993; Mendillo et al. 2016b).

The relative contribution of the above-mentioned heating processes to the electron temperature enhancement at sub-auroral latitudes and SAR arcs excitation should be quantitatively investigated in future studies.

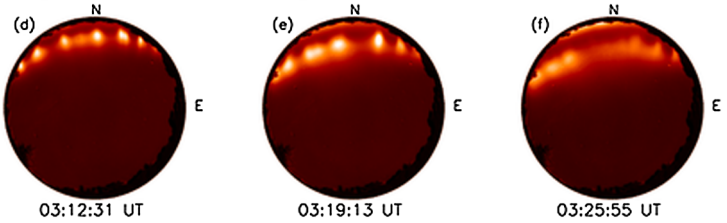


**Fig. 18** SAR arc with embedded structures observed on the night of 2 October 2013 at Millstone Hill. After ∼30 minutes, the beaded structures begin to dissipate and a 'regular' uniform arc is left (adapted from Mendillo et al. 2016a)

### 4.3 Departure from 'Stable' and 'Homogenous' SAR Arcs

Recent studies have shown that SAR arcs are far from being 'stable' structures and not all of them agree with the "classic" definition of a single east-west, geomagnetic latitude-aligned, uniform emission feature. Mendillo et al. (2016a) presented observations of a stable auroral red (SAR) arc observed from the Millstone Hill observatory that contained embedded substructures. Patches of emission occurred during a ∼30 min period in the pre-midnight sector that coincided with the main phase onset time of a moderate geomagnetic storm. Later in the evening, the pattern evolved into a classic SAR arc of uniform brightness east to west. Figure 18 shows these 'beaded' structures superimposed on the uniform arc. Several brightness peaks with average longitude spacing of ∼4° can be identified. Concurrent images in the oxygen green line (5577 Å) showed similar patches of emission but without a background arc. Observations of total electron content (TEC) from GPS satellites showed increases in TEC and phase fluctuations when the ray paths crossed the optical features. This case seems to represent an example of two emission mechanisms within a single SAR arc: a dominant level of emission due to thermal excitation, augmented by small bursts of soft energetic particles that excite additional 6300 Å radiation and 5577 Å. These observations led Mendillo et al. (2016a) to hypothesize that the inner edge of the plasma sheet (source of the soft precipitation that creates diffuse aurora) and the ring current-plasmapause interaction region (source of the downward heat flux that creates the SAR arc) occupied the same flux tube of 0.2 $R_E$ extent in the geomagnetic equatorial plane during the ∼30 min period when the beaded structures were observed.

Other morphological departures from single and 'stable arcs' are shown in Fig. 19. The left panel shows an image with two SAR arcs, representing the presence of two boundaries in the plasmasphere. Evidence of this kind of structuring seems to be possible as seen in Nishimura et al. (2019) who showed the presence of two separated ionospheric troughs and electron temperature peaks when looking at DMSP 17 data (see their Fig. 2a). The middle panel shows an arc with finger-like structures extending to the north, evidence of irregular and dynamic poleward boundaries. In the right panel, several small-scale patches of enhanced brightness are observed along the arc. The cases shown in Fig. 19 indicate that the assumption of a uniform Magnetosphere-Ionosphere interaction region needs to be reconsidered to take into account the non-uniform ionospheric response as a result of associated complex plasmapause/ionospheric trough boundaries.

## 5 STEVE

The discovery of a new phenomenon located several degrees equatorward from the auroral oval is an excellent example illustrating that new developments are still occurring in auroral

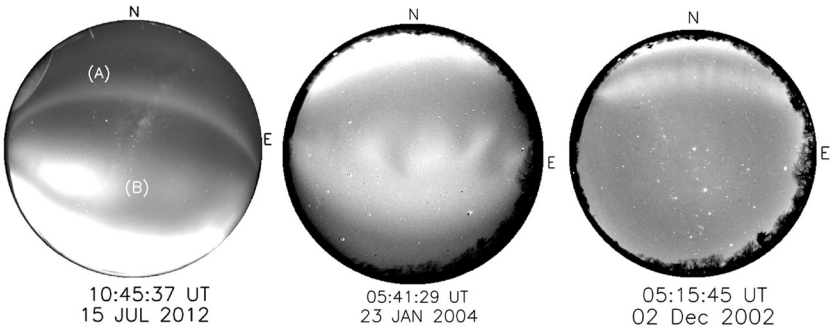


**Fig. 19** Examples of lack of uniformity observed during three different SAR arc events. (Left): A double SAR arc observed at Mount John in New Zealand; the arc closer to the diffuse aurora is brighter than that located equatorward. (Middle): Northward finger-like structures accompany the SAR arc observed at Millstone Hill. (Right): Several small-scale structures are seen within the SAR arc. (Figure adapted from Mendillo et al. 2016b)

and subauroral research. Amateur night sky watchers and auroral photographers have documented this upper atmospheric phenomenon for decades, but the scientific community only recently began analyzing it in further detail. The story of this discovery has been recently published by Gallardo-Lacourt et al. (2019).

Based on auroral photographers' observations, the optical structure appears as a narrow luminous mauve structure across the night sky over thousands of kilometers in the east-west direction. Due to the location of the emission (equatorward of the auroral oval), the phenomenon was initially incorrectly named 'proton arc'. Observers later changed the name to 'Steve', a denomination without physical implications. As described below, based on the observed characteristics of this phenomenon, the name 'Steve' was subsequently changed to Strong Thermal Emission Velocity Enhancement, or STEVE.

In 2018, MacDonald et al. reported a STEVE event for the first time in the scientific literature. One of the primary tasks in this study was to identify STEVE in the scientific optical dataset with the aid of amateur auroral photographer data. As observed in red-line All-Sky Imager (ASI) data, STEVE appeared adjacent to, and equatorward of, the aurora oval (i.e., in the subauroral region). During this event, the structure extended thousands of kilometers in the east-west direction but had a width of only tens of kilometers in latitude. Figure 20 shows the STEVE event observed on July 25, 2016 reported by MacDonald et al. (2018). The event lasted for about an hour while propagating from east to west, covering the entire longitudinal extent of the ASI.

In addition to STEVE, MacDonald et al. (2018) reported a green feature resembling a picket fence that is sometimes observed together with STEVE. This green structure had smaller longitudinal and latitudinal dimensions than STEVE.

At the same time of the STEVE observation, the Swarm-A satellite crossed the location of the emission corroborating that the structure was located in the subauroral region. In addition, Swarm-A revealed that the observed luminosity was collocated with a hot ($\sim$6000K electron temperature) stream of fast moving ($>$6 km/sec) plasma less than 50 km in north-south extent. In addition, Swarm-A measured a small magnetic field perturbation consistent with a small downward field-aligned current (FAC). This result suggested that STEVE may not be generated like auroral arcs, which are associated with upward FACs (downward or precipitating electrons) (Kamide and Akasofu 1976). Based on these observed characteristics, scientists converted "Steve" into the backronym of Strong Thermal Emission Velocity

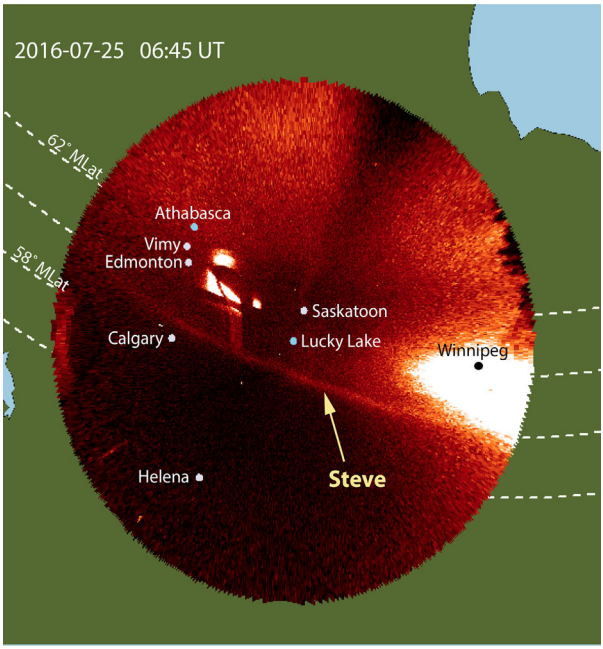


**Fig. 20** STEVE event reported by MacDonald et al. (2018) observed in REGO at Lucky Lake on July 25, 2016

Enhancement, or STEVE. As shown in Fig. 21, STEVE's maximum luminosity (Panel a) is collocated with fast moving ions (Panel b), extremely high electron temperature (Panel c), and the plasma trough (Panel d). The in-situ observations shown in Fig. 21 are consistent with a Subauroral Ion Drift (SAID); Archer et al. (2019a) recently corroborated the relationship between STEVE and extreme SAIDs which are characterized by faster moving ions, higher electron temperatures, and lower electron densities than regular SAIDs.

This initial case study by MacDonald et al. (2018) suggested STEVE to be fundamentally different from traditional aurora. Several studies over the next two years investigated STEVE with as many different instruments as possible in order to further our understanding of this phenomena.

### 5.1 STEVE'S Generation Mechanisms

In an attempt to understand the generation mechanism behind STEVE's formation, Gallardo-Lacourt et al. (2018a) analyzed data from the Polar Orbiting Environmental Satellite (POES)-17 for one STEVE event that occurred on March 28, 2008 and was identified by the Time History of Events and Macroscale Interactions during Substorm (THEMIS) ASI. Figure 22 shows energy flux for ions (left) and electrons (right) for this event. The trapped particle population (90° view angle) and precipitating particles (0° view angle) are in black and blue curves, respectively (except for panel j that only shows 0° and 30° view angle). The green vertical line indicates the time when the magnetic footprint of POES-17 crosses STEVE. For protons, there is no clear evidence of precipitating particles at the time of STEVE. The situation is similar for high energy electrons (>30 keV); however, for low energy particles (50 eV–1 keV) the detector captured a significant increase in the precipitating electron flux (several orders of magnitude) at the time of STEVE. Nevertheless, the authors reported that the integrated energy flux for this event is at least two orders of magnitude

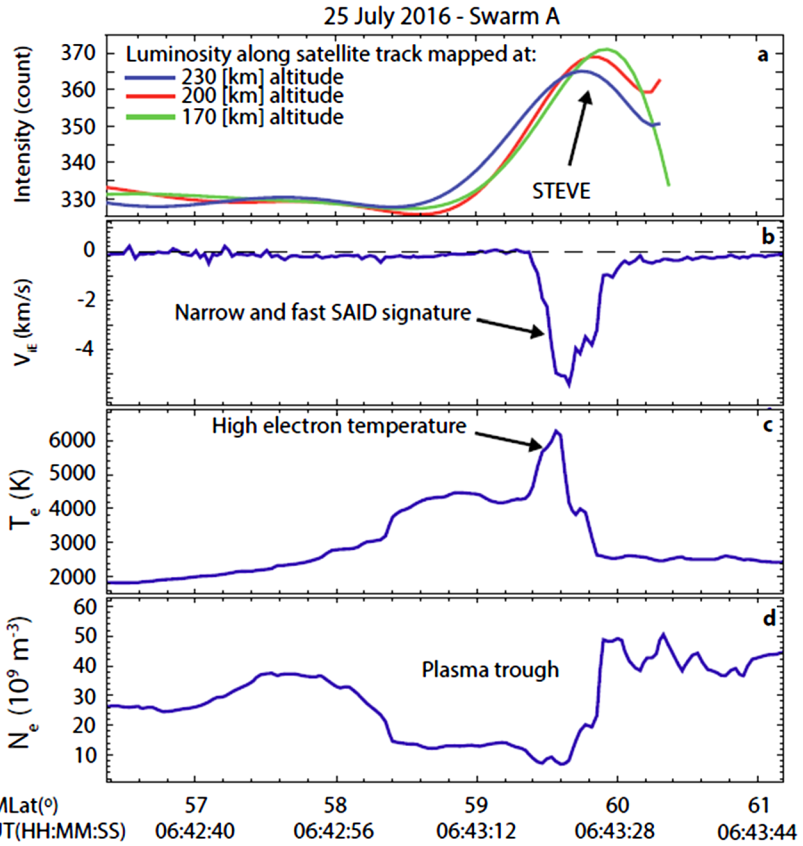


**Fig. 21** Swarm-A satellite crossing STEVE on July 25, 2016. Adapted from MacDonald et al. (2018)

smaller than the average energy fluxes reported for visible auroras (Zhang and Paxton 2008; Newell et al. 2010), concluding that these low precipitating energy fluxes cannot be responsible for the luminosity observed in STEVE.

This result suggests that STEVE is not produced by particle precipitation similar to the aurora but generated locally in the ionosphere.

A more recent study by Nishimura et al. (2019) investigated the magnetospheric drivers of several STEVE events and the "picket fence" originally identified by MacDonald et al. (2018). Although the mauve emission observed in STEVE could be explained by F-region thermal emission (like in SAR arcs), this mechanism could not explain the green features observed in the picket fence. The authors analyzed the processes involved in the generation of both phenomena by using a combination of non-traditional data from citizen scientists' photographs, ground and space-based imagers, and satellite data. The study showed for the first-time conjugate features for STEVE in the two hemispheres by using citizen scientist data in the northern hemisphere and the first STEVE observation measured by the Special Sensor Ultraviolet Spectrographic Imager (SSUSI) instrument on board of DMSP F-17 satellite in the southern hemisphere. The reported absence of proton precipitation for these STEVE events supported previous findings and confirmed that STEVE does not correspond to proton precipitation or a proton arc. The authors also reported that the picket fence struc-

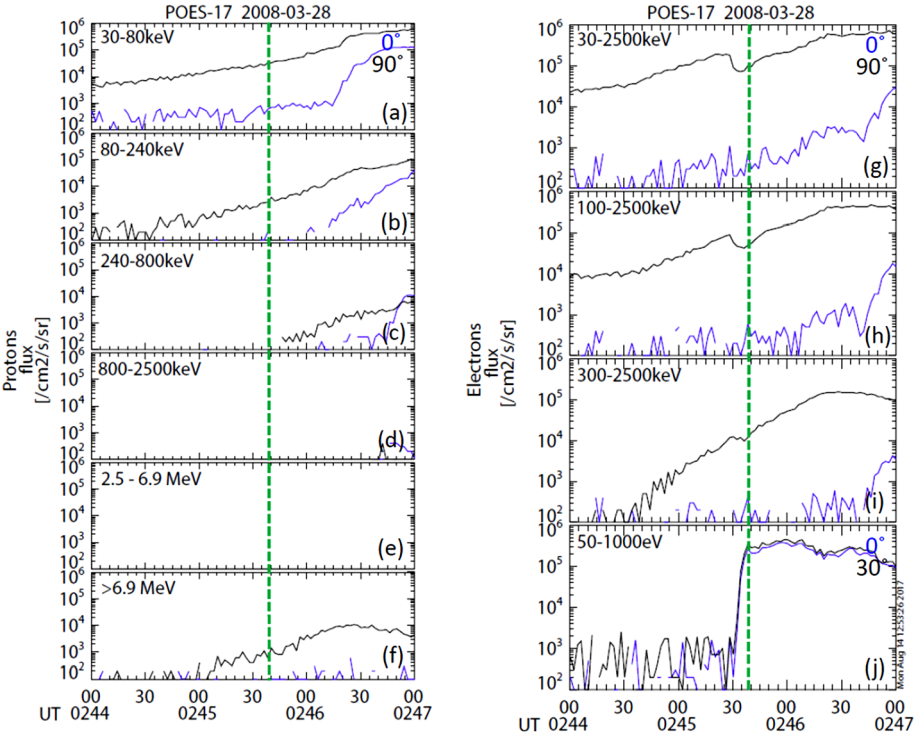


**Fig. 22** POES-17 satellite particle data. Proton (left) and electron (right) flux. (From Gallardo-Lacourt et al. 2018a)

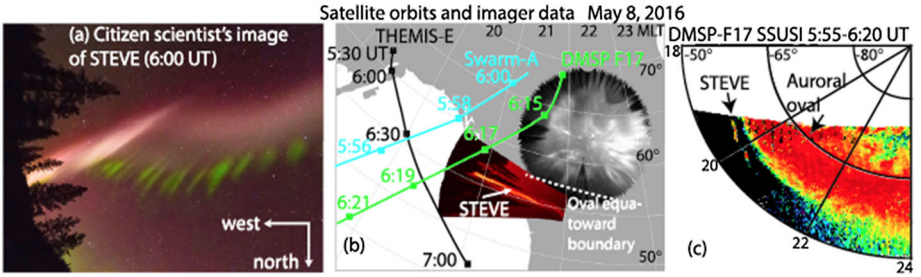


**Fig. 23** STEVE event observed in the northern and southern hemisphere together with a picket fence occurring on 8 May 2016. (**a**) Citizen scientist observation at the West Coast of North America. (**b**) REGO ASI observed STEVE at the Lucky Lake station, while THEMIS ASI measures auroral activity at higher latitude. (**c**) SSUSI instrument on board of DMSP F-17 detected the STEVE arc in the southern hemisphere. Figure adapted from Fig. 1 by Nishimura et al. 2019

ture was associated with electron precipitation of the order of 10 keV and weak upward Field-aligned current (FAC). Figure 23 has been adapted from Nishimura et al. (2019) and shows a STEVE event and picket fence occurring on 8 May 2016.

According to Nishimura et al. (2019), electron precipitation was only observed for events where the picket fence was present; in absence of the green-rayed structure no electron

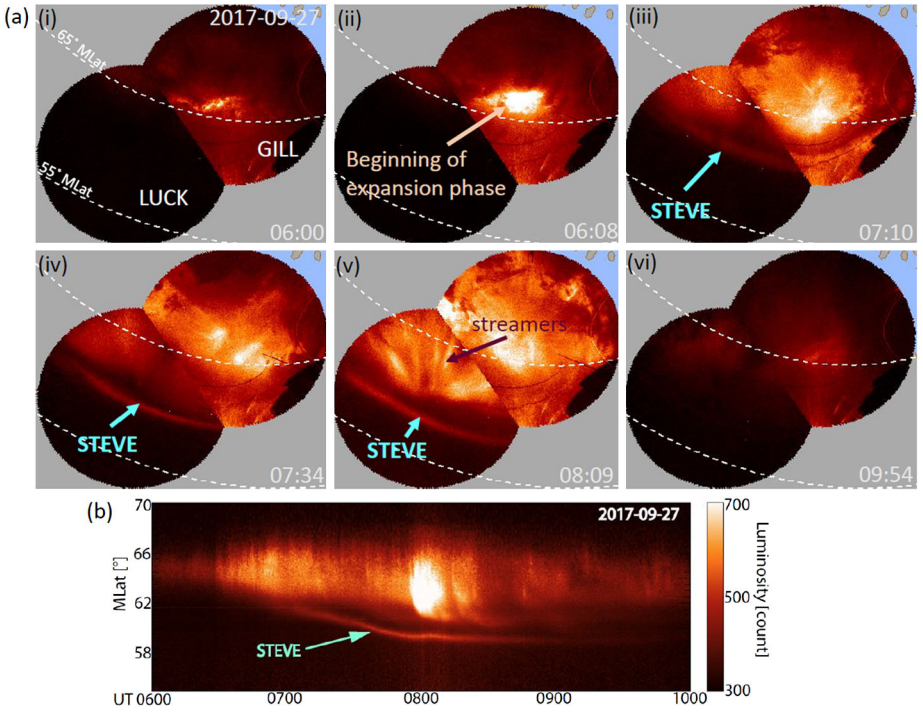


**Fig. 24** STEVE event captured with REGO ASI at Lucky Lake (LUCK) on September 27, 2017. (**a**) STEVE is a narrow structure located equatorward of the auroral oval. In this event, STEVE lasted about 2 hours. (**b**) Keogram with STEVE event showing the structure's equatorward displacement. (From Gallardo-Lacourt et al. 2018b)

precipitation was detected. These observations support previous findings establishing that STEVE is locally produced in the ionosphere, but also suggest that the picket fence structure is formed by electron precipitation, which is an auroral-like process. In addition, the authors reported observations of waves and strong electric fields that could be responsible for producing heating in the F region ionosphere, as well as a structured electron boundary that may drive precipitation for the picket fence structure.

## 5.2 STEVE's Morphology and Geomagnetic Conditions

Gallardo-Lacourt et al. (2018b) reported a statistical analysis of STEVE's properties for 28 STEVE events identified in two optical data bases (THEMIS and REGO ASI) from December 2007 to December 2017. They reported that all the events occurred between 22-01 MLT and on average STEVE lasted for about one hour and its latitudinal width was ∼20 km. STEVE also showed a latitudinal displacement (equatorward for most of the events) of about 50 km on average during its entire duration. STEVE's longitudinal extent was ∼2145 km across the North American sector, limited by the ASI field-of view. Figure 24 shows an example of the STEVE events analyzed by Gallardo-Lacourt et al. (2018a, 2018b). STEVE lasted about 2 hours and covered the entire FOV of the ASI. The keogram (panel b) illustrates the equatorward motion that was typically observed for STEVE events.

Gallardo-Lacourt et al. (2018b) analyzed magnetosphere and solar wind data to investigate the geomagnetic conditions under which STEVE develops. The Dst index for the events

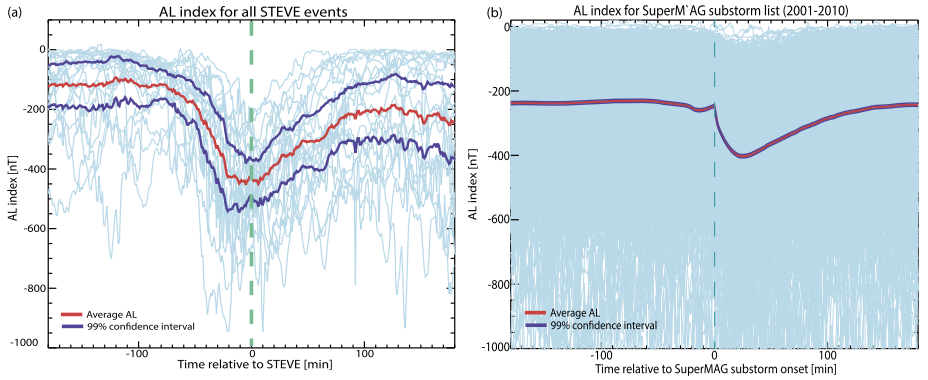


**Fig. 25** AL-index for 28 STEVE events (left) and for SuperMAG substorms (right). Adapted from Gallardo-Lacourt et al. (2018b)

was relatively moderate at ∼20 nT and Kp increased from 2 to 3.5 about 12 hours before STEVE was observed. In addition, the average solar wind speed and dynamic pressure were ∼550 km/s and ∼3 nPa, respectively.

From a superposed epoch analysis of AL index, the STEVE events reported in the study occurred about 1 hour after substorm onset at the end of a prolonged expansion phase. Figure 25 (adapted from Gallardo-Lacourt et al. 2018b) shows the AL index for the STEVE events (left panel) and the average AL index for the 16k substorms from the SuperMAG database. This result suggested that for STEVE to be observed, large amount of plasma may be injected from the magnetotail towards the inner magnetosphere. It is possible these injections effectively increase the ring current pressure and further enhance the subauroral westward flows, an effect that is consistent with the Swarm observations from MacDonald et al. (2018) and Archer et al. (2019a).

Recently, Archer et al. (2019b) analyzed photographers' data to estimate the altitude at which STEVE and the picket fence are produced. They used triangulation to analyze one event in which both structures were observed. They concluded that the picket fence was located from roughly 95- to 150-km altitude and STEVE to range from roughly 130- to 270-km altitude. During this event, they suggested that STEVE and the picket fence were aligned with each other along similar magnetic field lines. Figure 26 shows (a) the estimated altitudes for STEVE and the picket fence and (b) the median brightness for the red, green and blue channels, for the photograph in panel a. The authors highlighted that these qualitative observations should be interpreted with caution as the photographs have not been color calibrated for scientific purposes.

### 5.3 STEVE's Spectrum

Recent observations using an imaging spectrograph from the recently deployed Transition Region Explorer (TREx) array showed the spectrum of the picket fence and STEVE for the first time (Gillies et al. 2019). The spectrograph is designed to capture nighttime aeronomical phenomena with emissions between 400–800 nm, with a resolution of 0.4 nm.

Figure 27 shows the picket fence spectrum. The blue curve corresponds to the luminosity of the picket fence and the green (red) line corresponds to the background luminosity poleward (equatorward) of the picket fence structure, as shown in the inset. The location of the picket fence was obtained by fitting a Gaussian curve to the luminosity profile and the

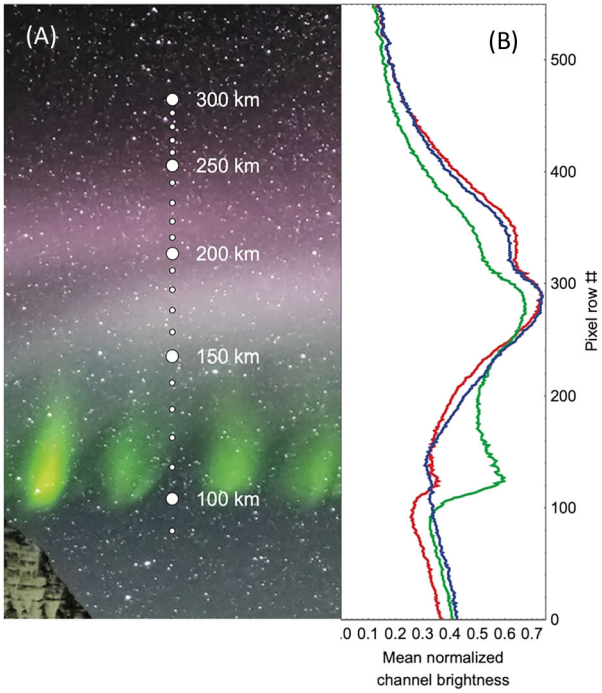


**Fig. 26** (**a**) Estimated altitude for STEVE event and picket fence on 16 September 2017. (**b**) Median brightness from red, blue and green channels for each row of pixels in panel a. Adapted from Archer et al. (2019b)

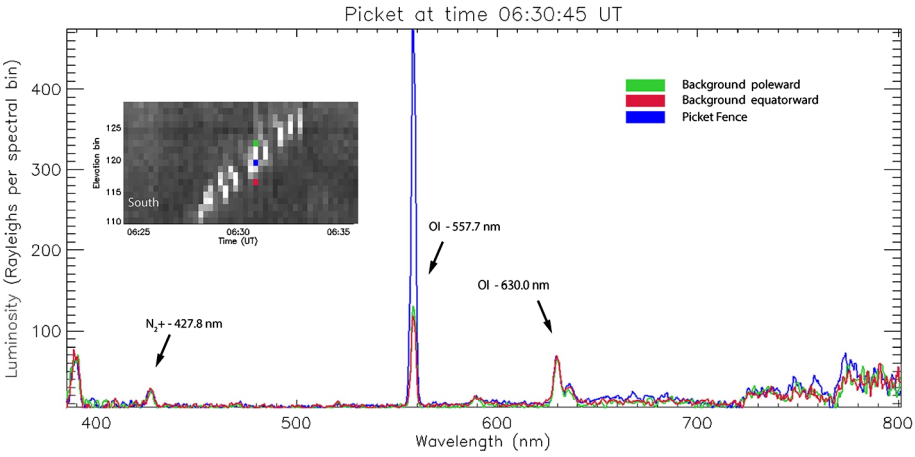


**Fig. 27** Spectrum of picket fence structure obtained using the Transition Region Explorer (TREx) imaging spectrograph. Inset shows the locations where the respective luminosities were extracted. Adapted from Gillies et al. (2019)

background was defined by extracting the luminosity at $3\sigma$ poleward and equatorward. Figure 27 shows that the blue line (picket fence) clearly differs from the background at 557.7 nm which corresponds to the green line emission. The authors concluded that the picket fence is dominated by OI 557.7 emission with intensities higher than the normal level of airglow, indicating that the picket fence is likely produced by electron precipitation.

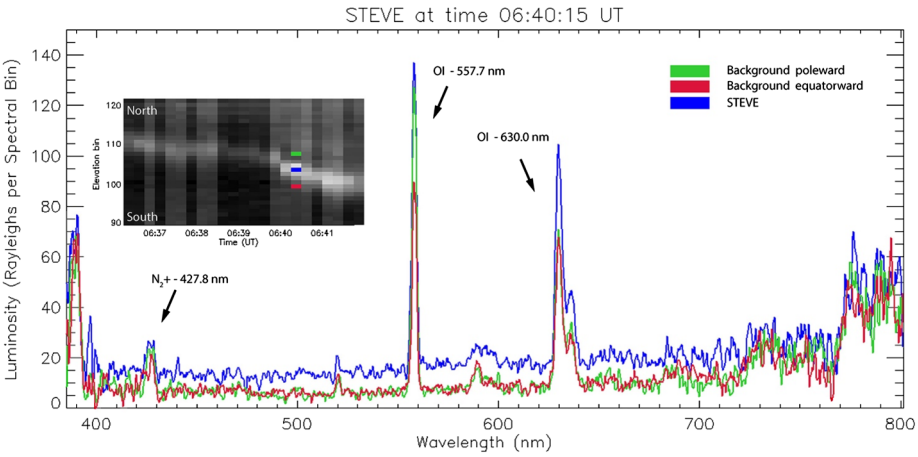


**Fig. 28** STEVE spectrum obtained with the TREX imaging spectrograph. Adapted from Gillies et al. (2019)

The Gillies et al. (2019) study also presented a STEVE spectrum. The methodology to obtain STEVE and the background luminosity was similar to the one applied to the picket fence described above. The blue line in Fig. 28 shows STEVE's spectrum. The green and red lines indicate the background luminosities poleward and equatorward, respectively. STEVE spectrum shows an elevated emission continuum at all wavelengths, with slightly higher intensity at ∼630.0 nm emission. The total luminosity of STEVE was approximately 6 kR higher than the background. The authors concluded that STEVE's spectrum contains two major contributing components: the OI red-line doublets (630.0 and 636.4 nm) and an overall enhancement of a continuous spectrum spanning between ∼400 and 730 nm. The 557.7-nm green-line emission within STEVE only contributes a minor portion to the total STEVE brightness and is comparable to the night airglow intensity. Finally, Gillies et al. (2019) asserted that the observations essentially exclude STEVE from being an auroral phenomenon, consistent with previous studies (Gallardo-Lacourt et al. 2018a; Nishimura et al. 2019).

## 6 Outstanding Issues

Although much progress has been made to understand the structures at subauroral latitudes, there are several unresolved issues. For proton aurora for example, understanding the mechanism that produces proton scattering in the magnetosphere will give us important information about the interaction between the central plasma sheet and the inner magnetosphere. Some of these important open questions are for example: What are the differences between the electron and proton aurora spots? Which particular wave-particle interaction processes lead to the precipitation of protons?

In the subauroral region, several questions remain unanswered. Regarding SAR arcs, the mechanism responsible for the generation of energy that produces SAR arcs is not fully understood. The role that SAPS play on the formation of SAR arcs is still a topic under investigation. In addition, more studies are necessary to know how often, and under what conditions, sub-structures within SAR arcs develop. With respect to STEVE, although its spectrum has been analyzed, we do not understand the underlying chemistry playing a role

in its formation at the predicted altitudes. In addition, the physical mechanisms responsible for the optical signature of STEVE have not yet been identified and the relationship between STEVE and the picket fence phenomenon is still unknown. Lastly, even though STEVE and SAR are observed at similar latitudes, it is not known if or how STEVE can be related to SAR arcs.

In general, the overarching question regarding all subauroral phenomena relates to their potential commonality and their specific differences. Although the subauroral structures discussed in this chapter share a similar location with respect to the auroral oval, it is not known whether they are generated by the same wave-particle processes. The development of new ground-based observatories, together with simulation studies, would help advance our understanding of proton aurora and the optical structures in the subauroral regions. In addition, new satellite missions, both planned and under development, will bring a clearer understanding and complete view of the highly coupled system at these latitudes.

**Acknowledgements** B. Gallardo-Lacourt wants to thank Mei-Ching Fok for her invaluable thoughts and discussions related to this topic. C. Martinis thanks Wen Li and Qianli Ma for valuable inputs when discussing VAP data. H.U. Frey was supported by the NSF award AGS-1004736 and NASA's Explorers Program through contracts NNG12FA45C and NNG12FA42I. B. Gallardo-Lacourt was supported by a NASA postdoctoral program fellowship. C. Martinis was supported by NASA grant 80NSSC19K0546 issued through the Heliophysics Guest Investigator Program and by NSF Aeronomy and Office of Polar Program award #1246423'. We acknowledge the Van Allen probes data from the EMFISIS instrument obtained from http://emfisis.physics.uiowa.edu/Flight/, and data from the HOPE instrument obtained from http://www.rbsp-ect.lanl.gov/data_pub/.



## References

B.J. Anderson, R.E. Erlandson, L.J. Zanetti, A statistical study of Pc 1-2 magnetic pulsations in the equatorial magnetosphere, 1. Equatorial occurrence distributions. J. Geophys. Res. **97**, 3075 (1992)

C.D. Anger, M.C. Moshupi, D.D. Wallis, J.S. Murphree, L.H. Brace, G.G. Shepherd, Detached auroral arcs in the trough region. J. Geophys. Res. **83**(A6), 2683–2689 (1978). https://doi.org/10.1029/JA083iA06p02683

W.E. Archer, B. Gallardo-Lacourt, G.W. Perry, J.-P. St.-Maurice, S.C. Buchert, E.F. Donovan, Steve: the optical signature of intense subauroral ion drifts. Geophys. Res. Lett. **46**, 6279–6286 (2019a). https://doi.org/10.1029/2019GL082687

W.E. Archer, J.-P. St.- Maurice, B. Gallardo-Lacourt, G.W. Perry, C.M. Cully, E. Donovan et al., The vertical distribution of the optical emissions of a Steve and picket fence event. Geophys. Res. Lett. **46**, 10719–10725 (2019b). https://doi.org/10.1029/2019GL084473

J.L. Burch, W.S. Lewis, T.J. Immel, P.C. Anderson, H.U. Frey, S.A. Fuselier, J.-C. Gerard, S.B. Mende, D.G. Mitchell, M.F. Thomsen, Interplanetary magnetic field control of afternoon-sector detached proton auroral arcs. J. Geophys. Res. **107**, SMP 17 (2002). https://doi.org/10.1029/2001JA007554

J.W. Chamberlain, *Physics of the Aurora and Airglow* (Academic Press, New York, 1961). https://doi.org/10.1029/SP041

L.B.N. Clausen et al., Large-scale observations of a subauroral polarization stream by midlatitude SuperDARN radars: Instantaneous longitudinal velocity variations. J. Geophys. Res. **117** (2012). https://doi.org/10.1029/2011JA017232

K.D. Cole, Stable auroral red arc, sinks for energy of Dst main phase. J. Geophys. Res. **70**, 1689 (1965)

J.M. Cornwall, F.V. Coroniti, R.M. Thorne, Unified theory of SAR-arc formation at the plasmapause. J. Geophys. Res. **76**, 4428 (1971)

J.D. Craven, L.A. Frank, K.L. Ackerson, Global observations of a SAR ARC. Geophys. Res. Lett. **9**, 961–964 (1982). https://doi.org/10.1029/GL009i009p00961

M. de Soria-Santacruz, M. Spasojevic, L. Chen, EMIC waves growth and guiding in the presence of cold plasma density irregularities. Geophys. Res. Lett. **40**, 1940–1944 (2013). https://doi.org/10.1002/grl.50484

E. Donovan, E. Spanswick, J. Liang, J. Grant, B. Jackel, M. Greffen, Magnetospheric dynamics and the proton aurora, in *Auroral Phenomenology and Magnetospheric Processes: Earth and Other Planets*. Geophysical Monograph Series, vol. 197 (2012). https://doi.org/10.1029/2012GM001241

Y. Ebihara, G.V. Khazanov, Ring current, in *Space Weather Fundamentals*, ed. by G.V. Khazanov (CRC Press, Boca Raton, 2016), pp. 149–172. https://doi.org/10.1201/9781315368474

A. Egeland, W.J. Burke, Auroral hydrogen emissions: a historical survey. Hist. Geo- Space Sci. **10**, 201–213 (2019). https://doi.org/10.5194/hgss-10-201-2019

X. Fang, M.W. Liemohn, J.U. Kozyra, S.C. Solomon, Quantification of the spreading effect of auroral proton precipitation. J. Geophys. Res. **109**, A04309 (2004). https://doi.org/10.1029/2003JA010119

M.-C. Fok, J.U. Kozyra, L.H. Brace, Solar cycle variation in the subauroral electron temperature enhancement: comparison of AE-C and DE 2 satellite observations. J. Geophys. Res. **96**(A2), 1861–1866 (1991). https://doi.org/10.1029/90JA02377

M.C. Fok, J.U. Kozyra, A.F. Nagy, C.E. Rasmussen, G.V. Khazanov, Decay of equatorial ring current ions and associated aeronomical consequences. J. Geophys. Res. **98**(A11), 19381–19393 (1993). https://doi.org/10.1029/93JA01848

J.C. Foster, W.J. Burke, SAPS: a new categorization for sub-auroral electric fields. Eos Trans. AGU **83**(36), 393 (2002). https://doi.org/10.1029/2002EO000289

J.C. Foster, H.B. Vo, Average characteristics and activity dependence of the subauroral polarization stream. J. Geophys. Res. **107**(A12), 1475 (2002). https://doi.org/10.1029/2002JA009409

J.C. Foster, M.J. Buonsanto, M. Mendillo, D. Nottingham, F. Rich, W. Denig, Coordinated stable auroral red arc observations: relationship to plasma convection. J. Geophys. Res. **99**(A6), 11429–11439 (1994). https://doi.org/10.1029/93JA03140

B.J. Fraser, T.M. Loto'aniu, H.J. Singer, K. Takahashi, P.J. Chi, R.E. Denton, R.L. Lysak, Electromagnetic ion cyclotron waves in the magnetosphere, in *Magnetospheric ULF Waves: Synthesis and New Directions*, Chapman Conference on Magnetospheric ULF Waves. Geophysical Monograph Book Series, vol. 169 (2006), pp. 195–212. https://doi.org/10.1029/169GM13

H.U. Frey, Localized aurora beyond the auroral oval. Rev. Geophys. **45**, RG1003 (2007). https://doi.org/10.1029/2005RG000174

H.U. Frey, S.B. Mende, T.J. Immel, J.-C. Gerard, B. Hubert, S. Habraken, J. Spann, G.R. Gladstone, D.V. Bisikalo, V.I. Shematovich, Summary of quantitative interpretation of IMAGE far ultraviolet auroral data. Space Sci. Rev. **109**, 255–283 (2003). https://doi.org/10.1023/B:SPAC.0000007521.39348.a5

H.U. Frey, G. Haerendel, S.B. Mende, W.T. Forrester, T.J. Immel, N. Ostgaard, Sub-Auroral Morning Proton Spots (SAMPS) as a result of plasmapause-ring-current interaction. J. Geophys. Res. **109**(A10), A10304 (2004). https://doi.org/10.1029/2004JA010516

M. Galand, S. Chakrabarti, Proton aurora observed from the ground. J. Atmos. Sol.-Terr. Phys. **68**, 1488–1501 (2006). https://doi.org/10.1016/j.jastp.2005.04.013

M. Galand, D. Lummerzheim, Contribution of proton precipitation to space-based auroral FUV observations. J. Geophys. Res. **109**, A03307 (2004). https://doi.org/10.1029/2003JA010321

B. Gallardo-Lacourt, J. Liang, Y. Nishimura, E. Donovan, On the origin of STEVE: particle precipitation or ionospheric skyglow? Geophys. Res. Lett. **45**, 7968–7973 (2018a). https://doi.org/10.1029/2018GL078509

B. Gallardo-Lacourt, Y. Nishimura, E. Donovan, D.M. Gillies, G.W. Perry, W.E. Archer et al., A statistical analysis of STEVE. J. Geophys. Res. Space Phys. **123**, 9893–9905 (2018b). https://doi.org/10.1029/2018JA025368

B. Gallardo-Lacourt, G.W. Perry, W.E. Archer, E. Donovan, How did we miss this? An upper atmospheric discovery named STEVE. Eos **100** (2019). https://doi.org/10.1029/2019EO117351

Y.I. Galperin, Polarization jet: characteristics and a model. Ann. Geophys. **20**(3), 391–404 (2002)

G.A. Germany, M.R. Torr, D.G. Torr, P.G. Richards, Use of FUV auroral emissions as diagnostic indicators. J. Geophys. Res. **99**, 383–388 (1994). https://doi.org/10.1029/93JA02357

D.M. Gillies, E. Donovan, D. Hampton, J. Liang, M. Connors, Y. Nishimura et al., First observations from the TREx spectrograph: the optical spectrum of STEVE and the picket fence phenomena. Geophys. Res. Lett. **46**, 7207–7213 (2019). https://doi.org/10.1029/2019GL083272

A. Hasegawa, K. Mima, Anomalous transport produced by kinetic Alfven wave turbulence. J. Geophys. Res. **83**, 1117 (1978)

J. Hong, J.-H. Kim, J.-K. Chung, Y.H. Kim, H. Kam, J. Park, M. Mendillo, Simultaneous observations of SAR arc and its ionospheric response at subauroral conjugate points (L $\simeq$ 2.5) during the St. Patrick's Day Storm in 2015. J. Geophys. Res. Space Phys. **125** (2020). https://doi.org/10.1029/2019JA027321

B. Hultqvist, H. Borg, P. Christophersen, W. Riedler, Observations of magnetic field-aligned anisotropy for 1 and 6 keV positive ions in the upper atmosphere. Planet. Space Sci. **19**, 279 (1971)

T.J. Immel, S.B. Mende, H.U. Frey, L.M. Peticolas, C.W. Carlson, J.-C. Gerard, B. Hubert, S.A. Fuselier, J.L. Burch, Precipitation of auroral protons in detached arcs. Geophys. Res. Lett. **29** (2002). https://doi.org/10.1029/2001GL013847

T. Iyemori et al., Localized injection of large-amplitude Pc 1 waves and electron temperature enhancement near the plasmapause observed in DE 2 in the upper atmosphere. J. Geophys. Res. **99**, 6187 (1994)

V.K. Jordanova, Ring current decay in the Quest for Space Weather Prediction (2020), pp. 181–223. https://doi.org/10.1016/B978-0-12-815571-4.00006-8

V.K. Jordanova, R.B. Torbert, R.M. Thorne, H.L. Collin, J.L. Roeder, J.C. Foster, Ring current activity during the early Bz < 0 phase of the January 1997 magnetic cloud. J. Geophys. Res. **104**(A11), 24895–24914 (1999). https://doi.org/10.1029/1999JA900339

V.K. Jordanova, M. Spasojevic, M.F. Thomsen, Modeling the electromagnetic ion cyclotron wave-induced formation of detached subauroral proton arcs. J. Geophys. Res. **112**, A08209 (2007). https://doi.org/10.1029/2006JA012215

Y. Kamide, S.-I. Akasofu, The location of the field-aligned currents with respect to discrete auroral arcs. J. Geophys. Res. **81**(22), 3999–4003 (1976). https://doi.org/10.1029/JA081i022p03999

J.U. Kozyra, E.G. Shelly, R.H. Comfort, L.H. Brace, T.E. Cravens, A.F. Nagy, The role of ring current $O^+$ in the formation of stable red arcs. J. Geophys. Res. **92**, 7487 (1987)

J.U. Kozyra, M.O. Chandler, D.C. Hamilton, W.K. Peterson, D.M. Klumpar, D.W. Slater, M.J. Buonsanto, H.C. Carlson, The role of ring current nose events in producing stable auroral red arc intensifications during the main phase: observations during the September 19-24, 1984 equinox transition study. J. Geophys. Res. **98**, 9267 (1993)

J.U. Kozyra, A.F. Nagy, D.W. Slater, High-altitude energy source(s) for stable auroral red arcs. Rev. Geophys. **35**, 155–190 (1997)

J. Krall, J.D. Huba, Plasmasphere, in *Space weather fundamentals*, ed. by G.V. Khazanov (CRC Press, Boca Raton, 2016), pp. 185–198. https://doi.org/10.1201/9781315368474

M. Kubota, T. Nagatsuma, Y. Murayama, Evening co-rotating patches: a new type of aurora observed by high sensitivity all-sky cameras in Alaska. Geophys. Res. Lett. **30** (2003). https://doi.org/10.1029/2002GL016652

L.J. Lanzerotti, A. Hasegawa, C.G. Maclennan, Hydromagnetic waves as a cause of a SAR arc event. Planet. Space Sci. **26**, 777 (1978)

S.R. LaValle, D.D. Elliott, Observations of SAR arcs from OV1-10. J. Geophys. Res. **77**(10) (1972)

J. Liang, E. Donovan, D. Gillies, E. Spanswick, M. Connors, Proton auroras during the transitional stage of substorm onset. Earth Planets Space **70**, 126 (2018). https://doi.org/10.1186/s40623-018-0899-0

V. Lobzin, A. Pavlov, Correlations between SAR arc intensity and solar and geomagnetic activity. Ann. Geophys. **17**, 770–781 (1999)

L. Lyons, Generation of large-scale regions of auroral currents, electric potentials, and precipitation by the divergence of the convection electric field. J. Geophys. Res. **85**(A1), 17–24 (1980). https://doi.org/10.1029/JA085iA01p00017

L.R. Lyons, Discrete aurora as the direct result of an inferred high-altitude generating potential distribution. J. Geophys. Res. **86**(A1), 1–8 (1981). https://doi.org/10.1029/JA086iA01p00001

MacDonald et al., New science in plain sight: Citizen scientists lead to the discovery of optical structure in the upper atmosphere. Sci. Adv. **4**(3) (2018). https://doi.org/10.1126/sciadv.aaq0030

C. Martinis, J. Baumgardner, J. Wroten, M. Mendillo, All-sky-imaging capabilities for ionospheric space weather research using geomagnetic conjugate point observing sites. Adv. Space Res. (2018). https://doi.org/10.1016/j.asr.2017.07.021

C. Martinis, J. Baumgardner, M. Mendillo, M.J. Taylor, T. Moffat-Griffin, J. Wroten, C. Sullivan, R. Macinnis, B. Alford, Y. Nishimura, First ground-based conjugate observations of Stable Auroral Red (SAR) Arcs, submitted. J. Geophys. Res. Space Phys. **124**(6), 4658–4671 (2019). https://doi.org/10.1029/2018JA026017

S.B. Mende, H. Heetderks, H.U. Frey, J.M. Stock, M. Lampton, S.P. Geller, R. Abiad, O.H.W. Siegmund, S. Habraken, E. Renotte, C. Jamar, P. Rochus, J.-C. Gerard, R. Sigler, H. Lauche, Far ultraviolet imaging from the IMAGE spacecraft: 3. Spectral imaging of Lyman alpha and OI 135.6 nm. Space Sci. Rev. **91**, 287–318 (2000). https://doi.org/10.1023/A:1005292301251

M. Mendillo, J. Baumgardner, J. Wroten, C. Martinis, S. Smith, K.-D. Merenda, T. Fritz, M. Hairston, R. Heelis, C. Barbieri, Imaging magnetospheric boundaries at ionospheric heights. J. Geophys. Res. Space Phys. **118**, 7294–7305 (2013). https://doi.org/10.1002/2013JA019267

M. Mendillo, R. Finan, J. Baumgardner, J. Wroten, C. Martinis, M. Casillas, A stable auroral red (SAR) arc with multiple emission features. J. Geophys. Res. Space Phys. **121**, 10,564–10,577 (2016a). https://doi.org/10.1002/2016JA023258

M. Mendillo, J. Baumgardner, J. Wroten, SAR arcs we have seen: evidence for variability in stable auroral red arcs. J. Geophys. Res. Space Phys. **121**, 245–262 (2016b). https://doi.org/10.1002/2015JA021722

E.V. Mishin, Interaction of substorm injections with the subauroral geospace: 1. Multispacecraft observations of SAID. J. Geophys. Res. **118**(9), 5782–5796 (2013). https://doi.org/10.1002/jgra.50548

M.C. Moshupi, L.L. Cogger, D.D. Wallis, J.S. Murphree, C.D. Anger, Auroral patches in the vicinity of the plasmapause. Geophys. Res. Lett. **4**, 37–40 (1977)
M.C. Moshupi, C.D. Anger, J.S. Murphree, D.D. Wallis, J.H. Whitteker, L.H. Brace, Characteristics of trough region auroral patches and detached arcs observed by ISIS 2. J. Geophys. Res. **84**, 1333–1346 (1979)
P.T. Newell, A.R. Lee, K. Liou, S.-I. Ohtani, T. Sotirelis, S. Wing, Substorm cycle dependence of various types of aurora. J. Geophys. Res. **115**, A09226 (2010). https://doi.org/10.1029/2010JA015331
Y. Nishimura, B. Gallardo-Lacourt, Y. Zou, E. Mishin, D.J. Knudsen, E.F. Donovan et al., Magnetospheric signatures of STEVE: implications for the magnetospheric energy source and interhemispheric conjugacy. Geophys. Res. Lett. **46**, 5637–5644 (2019). https://doi.org/10.1029/2019GL082460
T.P. O'Brien, M.B. Moldwin, Empirical plasmapause models from magnetic indices. Geophys. Res. Lett. **30**, 1152 (2003). https://doi.org/10.1029/2002GL016007
M. Ozaki, K. Shiokawa, Y. Miyoshi, R. Kataoka, M. Connors, T. Inoue, S. Yagitani, Y. Ebihara, C.-W. Jun, R. Nomura, K. Sakaguchi, Y. Otsuka, H.A. Uchida, I. Schofield, D.W. Danskin, Discovery of 1 Hz range modulation of isolated proton aurora at subauroral latitudes. Geophys. Res. Lett. **45**, 1209–1217 (2018). https://doi.org/10.1002/2017GL076486
V. Pierrard, J. Goldstein, N. Andre, V.K. Jordanova, Recent progress in physics-based models of the plasmasphere. Space Sci. Rev. **145**, 193–229 (2009). https://doi.org/10.1007/s11214-008-9480-7
E.I. Reed, J.E. Blamont, Observations of the conjugate SAR arcs of September 28-30, 1967. J. Geophys. Res. **79**(16), 2524–2525 (1974)
M.H. Rees, D. Luckey, Auroral electron energy derived from ratio of spectroscopic emissions 1. Model computations. J. Geophys. Res. **79**(34), 5181–5186 (1974). https://doi.org/10.1029/JA079i034p05181
M.H. Rees, R.G. Roble, Observations and theory of the formation of stable auroral red arcs. Rev. Geophys. **13**, 201 (1975)
F. Roach, J. Roach, Stable 6300 Å auroral arcs in mid-latitudes. Planet. Space Sci. **11**, 523–545 (1963)
K. Sakaguchi, K. Shiokawa, Y. Miyoshi, Y. Otsuka, T. Ogawa, K. Asamura, M. Connors, Simultaneous appearance of isolated auroral arcs and Pc 1 geomagnetic pulsations at subauroral latitudes. J. Geophys. Res. **113**, A05201 (2008). https://doi.org/10.1029/2007JA012888
K. Sakaguchi, Y. Miyoshi, E. Spanswick, E. Donovan, I.R. Mann, V. Jordanova, K. Shiokawa, M. Connors, J.C. Green, Visualization of ion cyclotron wave and particle interactions in the inner magnetosphere via THEMIS-ASI observations. J. Geophys. Res. **117**, A10204 (2012). https://doi.org/10.1029/2012JA018180
K. Sakaguchi, K. Shiokawa, Y. Miyoshi, M. Connors, Isolated proton auroras and Pc1/EMIC waves at subauroral latitudes, in *Auroral Dynamics and Space Weather*, ed. by Y. Zhang, L.J. Paxton. Geophysical Monograph, vol. 215 (Wiley, New York, 2016)
S. Sazykin, B.G. Fejer, Y.I. Galperin, L.V. Zinin, S.A. Grigoriev, M. Mendillo, Polarization jet events and excitation of weak SAR arcs. Geophys. Res. Lett. **29**(12), 1586 (2002). https://doi.org/10.1029/2001GL014388
F. Søraas, K.M. Laundal, M. Usanova, Coincident particle and optical observations of nightside subauroral proton precipitation. J. Geophys. Res. Space Phys. **118**, 1112–1122 (2013). https://doi.org/10.1002/jgra.50172
E. Spanswick, E. Donovan, L. Kepko, V. Angelopoulos, The magnetospheric source region of the bright proton aurora. Geophys. Res. Lett. **44**, 10,094–10,099 (2017). https://doi.org/10.1002/2017GL074956
M. Spasojevic, S.A. Fuselier, Temporal evolution of proton precipitation associated with the plasmaspheric plume. J. Geophys. Res. Space Phys. **114** (2009). https://doi.org/10.1029/2009JA014530
M. Spasojevic, H.U. Frey, M.F. Thomsen, S.A. Fuselier, S.P. Gary, B.R. Sandel, U.S. Inan, The link between a detached subauroral proton arc and a plasmaspheric plume. Geophys. Res. Lett. **31** (2004). https://doi.org/10.1029/2003GL018389
M. Spasojevic, M.F. Thomsen, P.J. Chi, B.R. Sandel, Afternoon subauroral proton precipitation resulting from ring current-plasmasphere interaction, in *Inner Magnetosphere Interactions: New Perspectives from Imaging*. Geophysical Monograph Series, vol. 159 (AGU, Washington, 2005)
R.W. Spiro, R.A. Heelis, W.B. Hanson, Rapid sub-auroral ion drifts observed by Atmospheric Explorer C. Geophys. Res. Lett. **6**, 657 (1979)
Y. Takagi, K. Shiokawa, Y. Otsuka, M. Connors, I. Schofield, Statistical analysis of SAR arc detachment from the main oval based on 11-year, all-sky imaging observation at Athabasca, Canada. Geophys. Res. Lett. **45**, 11,539–11,546 (2018). https://doi.org/10.1029/2018GL079615
S.A. Thaller, J.R. Wygant, L. Dai, A.W. Breneman, K. Kersten, C.A. Cattell, S.R. Bounds, Van Allen probes investigation of the large-scale duskward electric field and its role in ring current formation and plasmasphere erosion in the 1 June 2013 storm. J. Geophys. Res. Space Phys. **120**(6), 4531–4543 (2015). https://doi.org/10.1002/2014JA020875
N.A. Tsyganenko, Modeling the Earth's magnetospheric magnetic field confined within a realistic magnetopause. J. Geophys. Res. **100**(A4), 5599–5612 (1995). https://doi.org/10.1029/94JA03193

N.A. Tsyganenko, A model of the magnetosphere with a dawn-dusk asymmetry. 1. Mathematical structure. J. Geophys. Res. **107**(A8), SMP 12 (2002). https://doi.org/10.1029/2001JA000219

L. Vegard, Results of the investigations of the auroral spectrum during the years 1921–1926. Geofys. Publik. **9**, 1–71 (1932)

V.G. Vorobjev, O.I. Yagodkina, Comparative characteristics of ion and electron precipitation in the dawn and dusk sectors. Geomagn. Aeron. **54**, 50–58 (2014). https://doi.org/10.1134/S0016793214010162

B. Wang, P. Li, J. Huang, B. Zhang, Nonlinear Landau resonance between EMIC waves and cold electrons in the inner magnetosphere. Phys. Plasmas **26**(4), 042903 (2019)

A.G. Yahnin, T.A. Yahnina, Energetic proton precipitation related to ion-cyclotron waves. J. Atmos. Sol.-Terr. Phys. **69**, 1690–1706 (2007). https://doi.org/10.1016/j.jastp.2007.02.010

A.G. Yahnin, T.A. Yahnina, H.U. Frey, Subauroral proton spots visualize the Pc1 source. J. Geophys. Res. Space Phys. **112**, A10223 (2007). https://doi.org/10.1029/2007JA012501

A.G. Yahnin, T.A. Yahnina, H.U. Frey, T. Bosinger, J. Manninen, Proton aurora related to intervals of pulsations of diminishing periods. J. Geophys. Res. Space Phys. **114**, A12215 (2009). https://doi.org/10.1029/2009JA014670

A.G. Yahnin, T.A. Yahnina, H. Frey, V. Pierrard, Sub-oval proton aurora spots: mapping relatively to the plasmapause. J. Atmos. Sol.-Terr. Phys. **99**, 61–66 (2013). https://doi.org/10.1016/j.jastp.2012.09.018

T.A. Yahnina, A.G. Yahnin, Comparing the latitudinal distribution of the Pc1 intensity and the position of subauroral proton spots. Geomagn. Aeron. **52**, 624–628 (2012). https://doi.org/10.1134/S0016793212040159

J. Yao, Y. Cai, Y. Ma, S. Zhou, Evening corotating patches (ECP) observed by DMSP/SSUSI. J. Atmos. Sol.-Terr. Phys. **186**, 82–87 (2019). https://doi.org/10.1016/j.jastp.2019.02.008

Z.G. Yuan, X.H. Deng, X. Lin, Y. Pang, M. Zhou, P.M.E. Décréau, J.G. Trotignon, E. Lucek, H.U. Frey, J.F. Wang, Link between EMIC waves in a plasmaspheric plume and a detached sub-auroral proton arc with observations of Cluster and IMAGE satellites. Geophys. Res. Lett. **37** (2010). https://doi.org/10.1029/2010GL042711

Z. Yuan, M. Li, Y. Xiong, H. Li, M. Zhou, D. Wang, S. Huang, X. Deng, J. Wang, Simultaneous observations of precipitating radiation belt electrons and ring current ions associated with the plasmaspheric plume. J. Geophys. Res. Space Phys. **118**, 4391–4399 (2013). https://doi.org/10.1002/jgra.50432

Y. Zhang, L.J. Paxton, An empirical Kp-dependent global auroral model based on TIMED/GUVI data. J. Atmos. Sol.-Terr. Phys. **70**, 1231–1242 (2008)

Y. Zhang, L.J. Paxton, D. Morrison, B. Wolven, H. Kil, S. Wing, Nightside detached auroras due to precipitating protons/ions during intense magnetic storms. J. Geophys. Res. **110** (2005). https://doi.org/10.1029/2004JA010498

Y. Zou, Y. Nishimura, L.R. Lyons, E.F. Donovan, A statistical study of the relative locations of electron and proton auroral boundaries inferred from meridian scanning photometer observations. J. Geophys. Res. **117**, A06206 (2012). https://doi.org/10.1029/2011JA017357